Available online at www.sciencedirect.com
SCIENCE DIRECT
Icarus 181 (2006) 272–291
ICARUS
www.elsevier.com/locate/icarus

Simulations of dense planetary rings IV. Spinning self-gravitating particles with size distribution

Ryuji Morishima *, Heikki Salo

Department of Physical Sciences, Division of Astronomy, University of Oulu, P.O. Box 3000 FIN-90014, Finland

Received 12 May 2005; revised 17 September 2005

Available online 22 December 2005

Abstract

Previous self-gravitating simulations of dense planetary rings are extended to include particle spins. Both identical particles as well as systems with a modest range of particle sizes are examined. For a ring of identical particles, we find that mutual impact velocity is always close to the escape velocity of the particles, even if the total rms velocity dispersion of the system is much larger, due to collective motions associated to wakes induced by near-gravitational instability or by viscous overstability. As a result, the spin velocity (i.e., the product of the particle radius and the spin frequency) maintained by mutual impacts is also of the order of the escape velocity, provided that friction is significant. For the size distribution case, smaller particles have larger impact velocities and thus larger spin velocities, particularly in optically thick rings, since small particles move rather freely between wakes. Nevertheless, the maximum ratio of spin velocities between the smallest and largest particles, as well as the ratio for translational velocities, stays below about 5 regardless of the width of the size distribution. Particle spin state is one of the important factors affecting the temperature difference between the lit and unlit face of Saturn's rings. Our results suggest that, to good accuracy, the spin frequency is inversely proportional to the particle size. Therefore, the mixing ratio of fast rotators to slow rotators on the scale of the thermal relaxation time increases with the width of the particle size distribution. This will offer means to constrain the particle size distribution with the systematic thermal infrared observations carried by the Cassini probe.

Keywords: Planetary rings; Saturn; Collisional physics; Rotational dynamics

1. Introduction

This is the fourth paper describing our systematic study of the dynamics of dense planetary rings via local N-body simulations (see Salo, 1991, 1992a, 1995). In the present paper, we focus on the spin state of ring particles and the effect of friction on dynamical behavior of rings, based on simulations with spinning and self-gravitating particles with size distribution. The local kinetic steady-state of rings is determined by the balance between viscous gain from the tidal field and energy loss by inelastic collisions (e.g., Stewart et al., 1984). Friction modifies this balance since it enhances collisional dissipation and enables the transfer between the kinetic and rotational (spin) energies (e.g., Salo, 1987a; Araki, 1988). Similarly, there is a transfer of these energies between different sized particles, driving the system toward energy equipartition, although the complete equipartition is prevented by the dissipative nature of impacts (e.g., Salo, 1992a; Ohtsuki, 1999, 2005). Inclusion of self-gravity also modifies the steady-state, both via gravitational scattering in pairwise encounters and by increased viscosity induced by collective gravity wakes.

As long as we consider intrinsic evolution of rings, both random and spin energy can be scaled by $(r\Omega)^2$, where r and Ω stand for the particle radius and the orbital frequency, respectively. In the equilibrium state these scaled energies depend on five factors: (1) the elasticity of impacts represented by the coefficient of normal restitution ϵ_n, (2) the amount of friction in terms of the tangential restitution coefficient ε_t or the friction coefficient k_f, (3) the optical depth τ, (4) the strength of self-gravity via the r_p-parameter representing the ratio of physical radius to the Hill radius of the particle, and (5) the width of the size distribution $W = r_{max}/r_{min}$, where r_{max} and r_{min} represent

* Corresponding author. Current address: Institute for Mineralogy and Petrography, ETH Center, 8092 Zurich, Switzerland. Fax: +41 1 635 5704.
E-mail address: ryuji.morishima@erdw.ethz.ch (R. Morishima).

0019-1035/$ – see front matter
doi:10.1016/j.icarus.2005.10.023

the maximum and minimum radii of particles, respectively. We systematically examine the dependence of ring structure and spin state on these parameters, focusing on the effects of the friction and the width of the size distribution. Some preliminary results have already been reported in Morishima and Salo (2004b).

There exists numerous previous studies modeling the dynamics of planetary rings, and some of them have included the spins of particles and their size distribution. In the early studies, rings were mainly modeled based on the Boltzmann's equation. In the pioneering works—for rings with identical, non-self-gravitating, and frictionless particles—Goldreich and Tremaine (1978) and Hämeen-Anttila (1978) described the evolution of the tri-axial velocity dispersion ellipsoid and derived the critical coefficient of restitution, $\epsilon_{\rm crit}$, for which the viscous heating balances the collisional dissipation, as a function of τ. The slight difference of these two works results from the details of the averaging techniques for the collisional term (see reviews by Stewart et al., 1984, and by Salo, 2000). The model of Goldreich and Tremaine (1978) was later extended to include the effect of finite size of particles and the spin degree of freedom, both by Shukhman (1984) and by Araki (Araki and Tremaine, 1986; Araki, 1988, 1991). The model by Hämeen-Anttila (1978) was also extended to include the effect of finite size of particles, size distribution, and gravitational encounters between particle pairs in Hämeen-Anttila (1983, 1984) and later also their spins, in Salo (1987a) and Hämeen-Anttila and Salo (1993).

The evolution of orbital elements of ring particles were also calculated by using sets of three-body orbital integrations for interacting pairs (Petit and Hénon, 1987; Ohtsuki, 1999). Recently, based on three-body problem, the spin rate of a moonlet embedded in a swarm of much smaller ring particles is investigated by Morishima and Salo (2004a) and Ohtsuki (2004a, 2004b). Further, Ohtsuki (2005) investigated spin rate of ring particles with a broad size distribution by solving an evolution equation for rotational energy. These calculations, using three-body integrations, may be more precise than the above mentioned treatments based on the Boltzmann's equation, but are limited to an only optically thin case, $\tau \ll 1$. The analytic and numerical models based on the Boltzmann's equation or three-body integrations agree well with the results of N-body simulations described in the following, as long as the optical depth of a ring is sufficiently small so that collective motions due to ring self-gravity can be neglected.

N-body simulations complementing the analytical studies have also been conducted by several authors. In the early simulations, azimuthally complete rings were followed in an inertial coordinate system (Trulsen, 1972; Brahic, 1977; Lukkari, 1978; Hämeen-Anttila and Lukkari, 1980; Salo, 1985). Salo (1987b) included particle spins to N-body simulations and confirmed the consistency with his own theoretical work (Salo, 1987a) based on Hämeen-Anttila's formalisms. However, because of the limited number of particles, these early simulations were not able to treat high optical depth rings nor the realistic ring self-gravity.

On the other hand, the local simulation method, which was first developed by Wisdom and Tremaine (1988); see also Toomre and Kalnajs (1991), utilizing a coordinate system co-rotating with a ring, opened the way to treat dense rings with a fixed optical depth by applying periodic boundary condition. Later, this method have been used by many authors (Salo, 1991, 1992a, 1992b, 1995; Salo et al., 2001; Richardson, 1994; Mosqueira, 1996; Daisaka and Ida, 1999; Ohtsuki and Emori, 2000; Daisaka et al., 2001; Karjalainen and Salo, 2004; Ohtsuki and Toyama, 2005). In particular, extending the seminal work by Wisdom and Tremaine (1988), Salo (1991, 1992a) examined the effects of size distribution while still neglecting self-gravity and particle spins. In Salo (1992b), self-gravity of particles was first introduced in local simulations. The most prominent result obtained for dense self-gravitating rings was the formation of trailing particle wakes in systems near the threshold of gravitational instability (Salo, 1992b, 1995; Richardson, 1994; Daisaka and Ida, 1999). These wakes are analogues to Julian and Toomre (1966) stellar dynamical wakes excited around massive orbiting bodies (see also Huber and Pfenniger, 2001); the main difference is the dissipative nature of ring particles, making it possible for the wakes to attain a statistical steady-state. Convincing evidence for such structures has now been obtaining by the various measurements carried out by Cassini (Collwell et al., 2005; Nicholson et al., 2005; Ferrari et al., 2005). Later it was also shown that the strong increase in viscosity associated to self-gravity can promote viscous overstability (Salo et al., 2001; Daisaka et al., 2001), leading to systematic axisymmetric oscillations. Gravity wakes, as well as overstable oscillations, significantly enhance the velocity dispersion of ring particles. However, the particle spin state and the effect of size distribution have not yet been studied in detail for dense self-gravitating rings, although some studies briefly discussed these factors (Richardson, 1994; Salo, 1992b, 1995). Recently, Ohtsuki and Toyama (2005) has studied spin state of ring particles and their results are in principle consistent with ours, although the parameter they use and their method of analysis are somewhat different from ours.

The other important factor affecting ring dynamics is satellite perturbations. These perturbations maintain gaps, excite density and bending waves in rings and also confine isolated ringlets. Related to the formation mechanisms of these structures, there are many theoretical studies (e.g., Goldreich and Tremaine, 1982, and references therein; Shu et al., 1985), N-body simulations (Hänninen and Salo, 1992, 1994, 1995; Mosqueira, 1996; Lewis and Stewart, 2000, 2005; Seiss et al., 2005), kinematic models based on three-body integrations (e.g., Spahn et al., 1994) and hydrodynamic models (Spahn and Sremčević, 2000; Sremčević et al., 2002). Regardless of the nature of the formed structures, the velocity dispersion of ring particles is significantly enhanced by satellites. However, it has not yet been clarified whether the spin velocity dispersion is enhanced by satellite perturbations as well. Although we do not include satellite perturbations in our present simulations, we can gain some insight of the spin state under satellite perturba-

tions, through an analysis of the spins in wakes and oscillations induced by intrinsic instabilities.

Besides the effect on the dynamical behavior of rings, the spin state is one of the important factors determining the thermal infrared emission from the rings: a faster particle spin should result in a smaller temperature difference between the illuminated and unilluminated sides of the particle (e.g., Cuzzi et al., 1984). Thermal emission from rings was modeled by Kawata and Irvine (1975) and Kawata (1983) assuming a multilayer ring model, and by Aumann and Kieffer (1973), Froidevaux (1981), and Leyrat et al. (2003) for a monolayer model. In the former model the ring is assumed to be much thicker than the particle size whereas the ring thickness is the same as the particle size for the latter model. Both type of models seem to prefer slowly rotating particles, though there is a trade-off relation between the deduced spin rate and the assumed particle albedo. Previously, most of thermal infrared data were obtained by Earth-based observations. Therefore, early modeling studies concentrated on the temperature dependence on the ring opening angle, rather than that on the solar-phase angle: however, it is the latter which has a more direct connection with the spin state of ring particles. Currently the Cassini space probe is monitoring ring temperatures with various solar-phase angles. One of the central goals in this paper is to provide theoretical predictions concerning the dynamically plausible ring structure and particle spin states, useful for modeling of thermal infrared emission. Incorporation of both dynamical and thermal models is likely to be necessary for the proper interpretation of the observational data obtained and to-be-obtained by Cassini.

In Section 2, our simulation method is introduced. Results from dynamical simulations are shown in Section 3, while some implications to thermal observations are discussed in Section 4. Section 5 summarizes our conclusions.

2. Methods

The simulation method we use in the present study is the same as in Salo (1995) and Salo et al. (2001). We apply the local rotating coordinate system, and the linearized equation of motion (Hill's equation) is solved with periodic boundary conditions taking into account the differential shear in the radial direction. For self-gravity, forces from nearby particles (usually within a distance of 10 particle radii) are calculated directly while a three-dimensional FFT method is utilized for forces from more distant particles (except when using the instantaneous impact method explained below, in which case direct calculation of self-gravity is used for all particles). For a more detailed description of the local method, see the references mentioned above.

Two different methods for treatment of impacts are used in simulations, like in Salo (1995) (see also Morishima and Salo, 2004a). Either the impacts are described as instantaneous velocity changes of colliding bodies ("Instantaneous impact" method), or the particle motion through the impact is integrated after defining a model for the forces affecting between partly penetrating bodies ("Force method"). The force method is much more favorable in the case of dense self-gravitating systems where the concept of separate pairwise impacts is no longer applicable (Salo et al., 2001; Karjalainen and Salo, 2004). On the other hand, for low optical depth systems, or for non-self-gravitating systems both methods are applicable: in this case we mainly use the instantaneous impact method which is faster, and which has also been used in most previous studies. The difference between these methods appears also in the current context of particle spins, which requires the evaluation of the tangential velocity change for an impacting pair. Consider two spherical particles with masses m_1 and m_2, radii r_1 and r_2, positions $\mathbf{R}_1$, $\mathbf{R}_2$, velocities $\mathbf{v}_1$, $\mathbf{v}_2$, colliding with each other. In terms of the relative velocity $\mathbf{v}_\mathrm{r} = \mathbf{v}_2 - \mathbf{v}_1$, the velocity difference $\mathbf{u}$ at the contact point is given by

$$\mathbf{u} = \mathbf{v}_\mathrm{r} - \big[r_1(\boldsymbol{\omega}_1 - \boldsymbol{\Omega}) + r_2(\boldsymbol{\omega}_2 - \boldsymbol{\Omega})\big] \times \mathbf{n}, \tag{1}$$

where $\mathbf{n}$ is the unit vector in the direction of $\mathbf{R}_2 - \mathbf{R}_1$, $\boldsymbol{\omega}_1$, $\boldsymbol{\omega}_2$ are the spin angular velocity vectors of the particles in an inertial (non-rotating) coordinate system, and $\boldsymbol{\Omega}$ is the orbital angular velocity vector of the rotating coordinate system, respectively.

In the first method ("Instantaneous impact method"), the locations of impacting points are searched and the corresponding instantaneous velocity changes are calculated, based on the elasticity and friction of the impact. The post-collisional velocity difference $\mathbf{u}'$ is given by (Salo, 1987a; Richardson, 1994)

$$\mathbf{u}' = -\varepsilon_\mathrm{n}\mathbf{u}_\mathrm{n} + \varepsilon_\mathrm{t}\mathbf{u}_\mathrm{t}, \tag{2}$$

where ε_n and ε_t stand for the normal and tangential restitution coefficients, and $\mathbf{u}_\mathrm{n} = (\mathbf{u}\cdot\mathbf{n})\mathbf{n}$ and $\mathbf{u}_\mathrm{t} = \mathbf{u} - \mathbf{u}_\mathrm{n}$ are the normal and tangential components of the pre-collisional velocity difference at the contact point, respectively (note that in Salo (1995) ε_t was defined in a different manner, corresponding to our current $1 - \varepsilon_\mathrm{t}$). Assuming homogeneous spherical particles, with the moment of inertia $2/5 m_i r_i^2$ $(i = 1, 2)$, the changes of the relative velocity and the spin vectors are derived from the conservations of linear and angular momenta as

$$\mathbf{v}_1' - \mathbf{v}_1 = \frac{m_2}{m_1 + m_2}\left[(1 + \varepsilon_\mathrm{n})\mathbf{u}_\mathrm{n} + \frac{2}{7}(1 - \varepsilon_\mathrm{t})\mathbf{u}_\mathrm{t}\right], \tag{3}$$

$$r_1\boldsymbol{\omega}_1' - r_1\boldsymbol{\omega}_1 = \frac{m_2}{m_1 + m_2}\frac{5}{7}(1 - \varepsilon_\mathrm{t})\mathbf{n} \times \mathbf{u}_\mathrm{t}, \tag{4}$$

where $\mathbf{v}_1'$ and $\boldsymbol{\omega}_1'$ are the velocity and the spin vector of the particle 1 after the impact, respectively. The changes of the velocity and the spin vector of the particle 2 can be obtained by multiplying Eq. (3) with $-m_1/m_2$ and Eq. (4) with m_1/m_2, respectively.

In the second method ("Force method"), particle orbits are integrated through impacts, including additional visco-elastic forces arising between the slightly overlapping particles. The additional translational acceleration $\dot{\mathbf{v}}_{1,\mathrm{add}}$ and the spin evolution are given by

$$\dot{\mathbf{v}}_{1,\mathrm{add}} = \frac{m_2}{m_1 + m_2}\ddot{\xi}(\mathbf{n} - k_\mathrm{f}\mathbf{n}_\mathrm{t}), \tag{5}$$

$$\frac{\mathrm{d}(r_1\boldsymbol{\omega}_1)}{\mathrm{d}t} = -\frac{m_2}{m_1 + m_2}\frac{5}{2}k_\mathrm{f}\ddot{\xi}\mathbf{n} \times \mathbf{n}_\mathrm{t}, \tag{6}$$

with

$$\ddot{\xi} = \begin{cases} -\omega_0^2 \xi - \frac{\dot{\xi}}{s} & (\xi \geqslant 0), \\ 0 & (\xi < 0), \end{cases} \tag{7}$$

where $\xi = (r_1 + r_2) - |\mathbf{R}_2 - \mathbf{R}_1|$ is the penetration depth, k_f denotes the coefficient of friction, and $\mathbf{n}_\mathrm{t} = \mathbf{u}_\mathrm{t}/|\mathbf{u}_\mathrm{t}|$ is the unit vector pointing in the tangential direction. Note that in Morishima and Salo (2004a), we use differently defined coefficient of friction $\ell_\mathrm{f} = 7k_\mathrm{f}/2$. In the above, ω_0 is the undamped frequency of the harmonic impact force, and s is the characteristic time of damping, respectively. Fixing values of ω_0 (we use $\omega_0/\Omega = 200$ or 400), we can obtain the desired value of the normal coefficient of restitution ε_n with appropriate values of s (see Salo, 1995; Morishima and Salo, 2004a, in detail). Note that the evolutions of the velocity and the spin of the particle 2 can be obtained by multiplying the mass coefficients in the same manner as in the instantaneous impact method. During the numerical integration for an impact, the normal time step used for orbital motion (typically 10^{-3} orbital periods) is divided into small substeps (typically at least 20 steps for the duration of the impact). The self-gravitational force are calculated only in the beginning of the normal step, but extrapolated in substeps using a linear Taylor series expansion. This extrapolation in substeps is necessary in order to avoid accumulation of numerical errors in the case particle aggregates form (Karjalainen and Salo, 2004).

Comparing the normal and tangential components of velocity change in the impact given in Eqs. (3) and (5) the relation between the friction coefficient k_f and the tangential restitution coefficient ε_t is obtained as

$$k_\mathrm{f} = \frac{2}{7} \frac{(1-\varepsilon_\mathrm{t})}{(1+\varepsilon_\mathrm{n})} \frac{|\mathbf{u}_\mathrm{t}|}{|\mathbf{u}_\mathrm{n}|}, \tag{8}$$

where we assumed that the relative tangential direction $\mathbf{n}_\mathrm{t}$ does not change during an impact in Eq. (6). Equation (8) suggests that the relation between k_f and ε_t depends on the impact angle. If we assume that impact directions are random (valid for a multilayer system with velocity dispersion $\gg r\Omega$) the averaging over impacts yields (see Appendix A)

$$\sqrt{\langle \mathbf{u}_\mathrm{t}^2 \rangle / \langle \mathbf{u}_\mathrm{n}^2 \rangle} = \big(14/(9+5\varepsilon_\mathrm{t})\big)^{1/2}. \tag{9}$$

Thus, for frictionless particles the average velocity ratio is unity, but in the case of $\varepsilon_\mathrm{t} < 1$, the tangential velocities include a slight enhancement due to spins. Supulver et al. (1995) showed that the value of ε_t is about 0.9 for glancing 1 cm s^{-1} impacts of spherical particles, which indicates $k_\mathrm{f} \sim 0.02$. However, since in practice deviations from the spherical shape may also enhance the spin energy (Salo, 1987a, 1987b), the effective value of ε_t might in fact be smaller in actual rings (thus a larger k_f is plausible).

Fig. 1 shows comparison of the instantaneous impact method and our force method in terms of the velocity dispersion $c = \langle \mathbf{v}^2 \rangle^{1/2}$ and the dispersion of spin velocity $q = \langle (r\boldsymbol{\omega})^2 \rangle^{1/2}$, where $\mathbf{v}$ is the particle random velocity relative to the systematic Keplerian velocity. Here k_f used in the force method is converted into ε_t by Eq. (8) assuming Eq. (9) holds for the average $|\mathbf{n}_\mathrm{t}|/|\mathbf{u}_\mathrm{n}|$. For positive values of ε_t, both methods are very

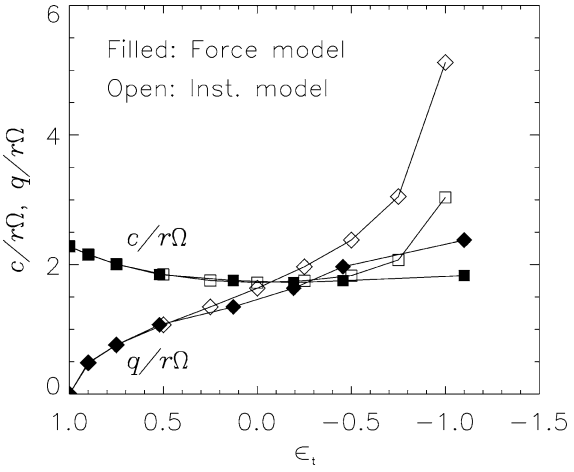

Fig. 1. Comparison of the instantaneous impact model and the force model. The translational and spin velocity dispersions, c and q, are shown as functions of the tangential restitution coefficient ε_t. For the force model, the friction coefficient k_f is converted into ε_t by using Eqs. (8) and (9) (note that Eq. (8) is valid only for positive ε_t: see the text). The optical depth of the system $\tau = 1.0$ and the coefficient of normal restitution $\varepsilon_\mathrm{n} = 0.5$. The self-gravity of particles is not taken into account.

well consistent with each other. The difference becomes evident for negative ε_t, where Eq. (8) is no longer applicable since the friction force vanishes in the force model when $\mathbf{u}_\mathrm{t}$ becomes zero during an impact, while the post-collisional $\mathbf{u}_\mathrm{t}$ can have the opposite direction to the pre-collisional direction in the instantaneous impact method. In other words, our force model cannot produce negative ε_t. However, it would be possible to produce a negative ε_t with our force method, if we hold the direction of the relative tangential velocity $\mathbf{n}_\mathrm{t}$ in Eq. (6) fixed to its initial value during the impact. Also, Brilliantov et al. (1996) described a more sophisticated impact model, which can produce negative, and impact velocity dependent, ε_t. Nevertheless, we do not apply it in the present paper as we keep the impact model as simple and transparent as possible.

Even if friction is not strong, differences between the two methods appear in some cases. Morishima and Salo (2004a) showed that the tangential velocity change for the instantaneous impact model is overestimated compared with the force model in the sliding phase, where multiple hits occur in a same particle pair with very small time intervals. This happens in rings with self-gravitating particles. As we show in the next section, similar differences owing to impact methods will appear for closely packed rings even without self-gravity.

3. Simulation results

3.1. Non-self-gravitating identical particles

Since most of previous studies based on the Boltzmann's equation treated identical particles, either neglecting altogether or including only approximately their self-gravity, we start from a non-self-gravitating identical particle case. Readers interested in more realistic applications may skip to Section 3.2. Differences between theoretical predictions and results obtained by N-body simulations are seen for closely packed rings with high

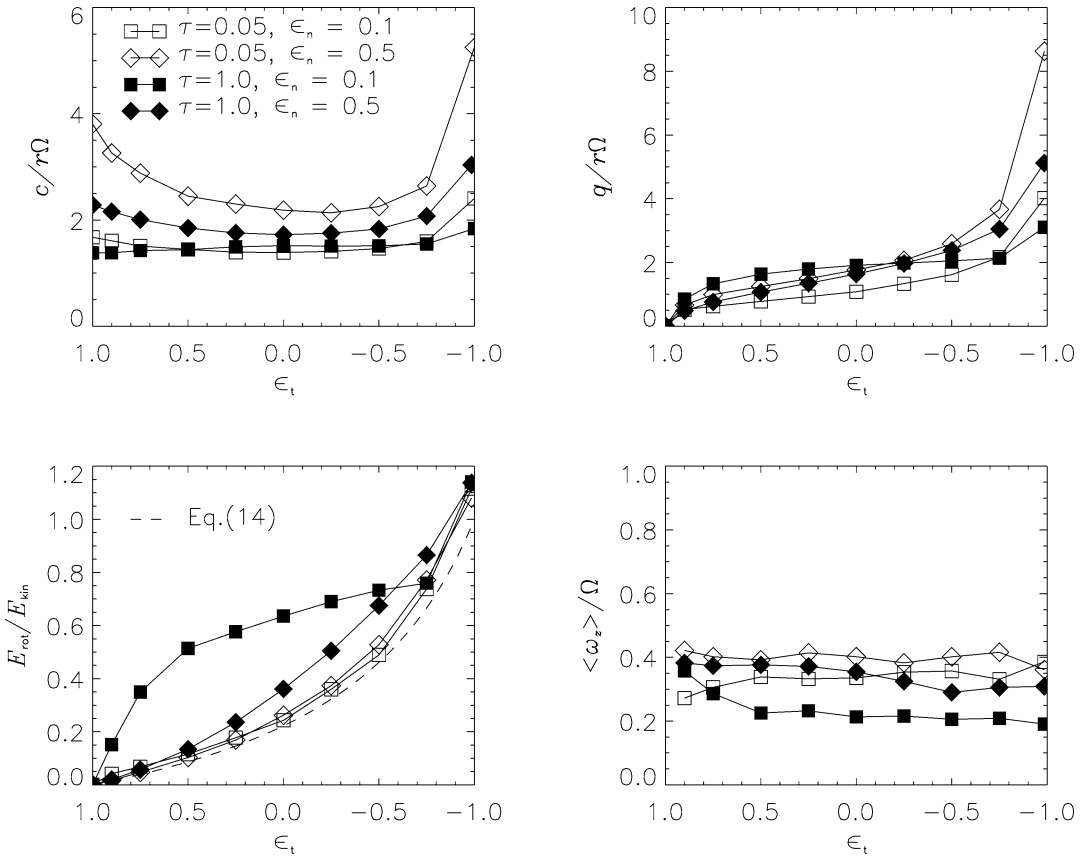

(a)

Fig. 2. (a) Dependence of physical properties on the tangential restitution coefficient ε_t, for the case of non-self-gravitating, identical particles. The instantaneous impact model is used. The dispersion of random velocity c, the dispersion of spin velocity q, the energy ratio E_{rot}/E_{kin}, and the z-component of the mean spin $\langle\omega_z\rangle$ are shown for four different cases (for low and moderate optical depth τ, combined with two values of the normal restitution coefficient ε_n). In the frame of E_{rot}/E_{kin}, the dashed curve represents the analytical prediction given by Eq. (14). (b) Continuation to (a). The coefficient of the local viscosity $\gamma_{local}/\tilde{\omega}_{c,eff}$, the coefficient of the non-local viscosity $\gamma_{non\text{-}local}/\tilde{\omega}_{c,eff}$, the normal component of the mean squared impact velocity $\langle\mathbf{u}_n^2\rangle$, and the effective collision frequency $\tilde{\omega}_{c,eff}$ are shown. The dashed line labeled GT represents the expected value of $\gamma_{local}/\tilde{\omega}_{c,eff} = 0.045$ from Goldreich and Tremaine (1978). The dashed lines denoted by 'multi' are the expected values of $\langle\mathbf{u}_n^2\rangle/c^2 = 4/3$ and $\tilde{\omega}_{c,eff} = \omega_{c,eff}/(\Omega\tau) \simeq 3$ from the multilayer approximation ($c \gg r\Omega$).

optical depth τ, and for small coefficient of normal restitution ε_n. On the other hand, theoretical predictions are consistent with the behavior of multilayer rings (velocity dispersion $c \gg r\Omega$).

Fig. 2a shows the velocity dispersion c, the dispersion of spin velocity q, the ratio of the rotational energy $E_{rot} = q^2/5$ to the kinetic energy $E_{kin} = c^2/2$, and the z-component of the mean spin rate $\langle\omega_z\rangle$ as functions of the tangential coefficient of friction ε_t for different τ and ε_n. The dispersion of the spin velocity increases monotonically with the friction strength $1-\varepsilon_t$, whereas the velocity dispersion has the minimum for $\varepsilon_t \sim 0.0$. The energy ratio is also a monotonically increasing function of $1-\varepsilon_t$ and is almost independent of τ and ε_n except for the most closely packed case with $\tau = 1.0$ and $\varepsilon_n = 0.1$. The mean spin rate ω_z is about 0.2–0.4 and is slightly smaller for larger τ cases.

3.1.1. Kinetic and rotational energies

In order to discuss the results in Fig. 2a more in detail, let us introduce a simple kinetic theory. The kinetic energy of rings is determined by the balance between viscous heating and collisional damping, whereas some kinetic energy is transferred to the rotation energy through mutual collisions of particles. The change rates of $E_{kin} = c^2/2$ and $E_{rot} = q^2/5$ are given by (e.g., Stewart et al., 1984; Shukhman, 1984; Araki, 1988)

$$\frac{dE_{kin}}{dt} = \frac{9}{4}\nu\Omega^2 + \Delta E_{kin}\omega_c, \tag{10}$$

$$\frac{dE_{rot}}{dt} = \Delta E_{rot}\omega_c, \tag{11}$$

where ν stands for the ring kinematic viscosity, ω_c for the collision frequency, ΔE_{kin} and ΔE_{rot} for the averaged changes of the kinetic and rotation energies in a collision both due to the dissipation and the exchange between these energies, respectively. In the multilayer approximation, where the velocity dispersion is large enough to justify the separate treatment of the random motion and the motion due to the systematic velocity field, the energy changes due to random motions are given by (Appendix A)

$$\Delta E_{kin} = -\frac{E_{kin}}{3}\left[\left(1-\varepsilon_n^2\right) + \frac{4}{7}(1-\varepsilon_t) - \frac{4}{49}(1-\varepsilon_t)^2\right] + \frac{10}{147}E_{rot}(1-\varepsilon_t)^2, \tag{12}$$

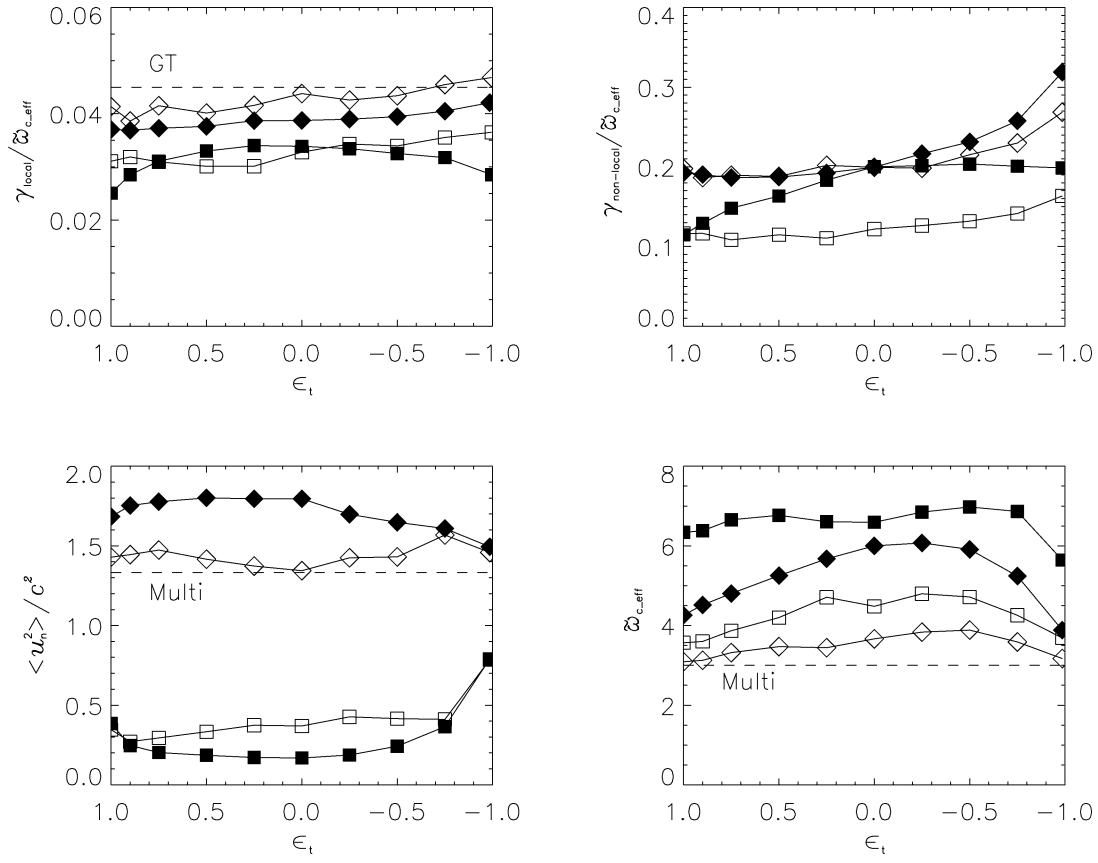

(b)

Fig. 2. (*continued*)

$$\Delta E_{\rm rot} = -\frac{5}{2}E_{\rm rot}\left[\frac{4}{21}(1-\varepsilon_{\rm t}) - \frac{10}{147}(1-\varepsilon_{\rm t})^2\right] + \frac{10}{147}E_{\rm kin}(1-\varepsilon_{\rm t})^2. \quad (13)$$

In the equilibrium state (d/d$t = 0$), from $\Delta E_{\rm rot} = 0$ the energy ratio can be obtained as (see also Salo, 1987a, 1987b; their $\beta \equiv 1 - \varepsilon_{\rm t}$)

$$\frac{E_{\rm rot}}{E_{\rm kin}} = \frac{2(1-\varepsilon_{\rm t})}{14 - 5(1-\varepsilon_{\rm t})}. \quad (14)$$

This equation suggests that the energy equipartition between rotation and random motion is achieved for $\varepsilon_{\rm t} = -1$. Equation (14) is shown in Fig. 2a as a dashed curve and found to be a very good approximation except for the most closely packed case. This special case will be discussed later. In the equilibrium state, $\Delta E_{\rm kin}$ can be also written in a simpler form

$$\Delta E_{\rm kin} = -\frac{E_{\rm kin}}{3}\left[(1-\varepsilon_{\rm n}^2) + \frac{2}{7}(1-\varepsilon_{\rm t}^2)\left(1 + \frac{5}{2}\frac{E_{\rm rot}}{E_{\rm kin}}\right)\right]. \quad (15)$$

The similar equations were also derived by Araki (1988). Substituting Eq. (14) into Eq. (15), it is found that $|\Delta E_{\rm kin}/E_{\rm kin}|$ becomes maximum for $\varepsilon_{\rm t} \simeq -0.30$ with fixed $\varepsilon_{\rm n}$. Indeed, the velocity dispersion usually has a minimum around this value of $\varepsilon_{\rm t}$ in Fig. 2a.

Though the dependences of the kinetic and rotational energies on $\varepsilon_{\rm t}$ and $\varepsilon_{\rm n}$ in Fig. 2a can be roughly explained by Eqs. (14) and (15), we need to take into account the functional dependencies of viscous gain in order to discuss the energy balance more accurately. For example, Eq. (15) suggests that the energy dissipation due to friction becomes zero both for $\varepsilon_{\rm t} = 1.0$ and -1.0, while the velocity dispersion for $\varepsilon_{\rm t} = -1.0$ is always higher than that for $\varepsilon_{\rm t} = 1.0$. Further, if we compare the cases with the different sets of $(\varepsilon_{\rm n}, \varepsilon_{\rm t})$ which give the same value of $|\Delta E_{\rm kin}/E_{\rm kin}|$ in Eq. (15), the velocity dispersion decreases with $\varepsilon_{\rm n}$ (for example, compare the cases of $(\varepsilon_{\rm n}, \varepsilon_{\rm t}) = (0.1, 1.0)$ and $(0.5, 0.5)$ in Fig. 2a). These facts suggest that the viscosity normalized by the collision frequency is an increasing function of $1 - \varepsilon_{\rm t}$ and $\varepsilon_{\rm n}$.

In the non-self-gravitating case, the viscosity is composed of the local and non-local viscosities $\nu = \nu_{\rm local} + \nu_{\rm non\text{-}local}$ (in the self-gravitating case, the gravitational viscosity is added to them; see Daisaka et al., 2001). The former one originates from momentum flow via random motion of particles whereas the latter is related to the momentum transfer across particles during collisions of finite sized particles. The form of the local viscosity is expected to be (Goldreich and Tremaine, 1978)

$$\nu_{\rm local} = \gamma_{\rm local}\frac{c^2}{\Omega}\frac{\tau}{1+\tau^2}, \quad (16)$$

and the expected form of the non-local viscosity is (Stewart et al., 1984; Daisaka et al., 2001)

$$\nu_{\rm non\text{-}local} = \gamma_{\rm non\text{-}local} r^2 \tau \Omega, \quad (17)$$

where $\gamma_{\rm local}$ and $\gamma_{\rm non\text{-}local}$ are numerical factors expected to be about 0.15 and 1.0, respectively. Substituting Eqs. (15)–(17) into Eq. (10) and divided by the collision frequency $\omega_{\rm c}$, which is proportional to τ in the non-self-gravitating case, the kinetic energy balance equation in the equilibrium state becomes

$$0 = \frac{9}{4}\frac{\gamma_{\rm local}}{\tilde{\omega}_{\rm c}}\frac{c^2}{1+\tau^2} + \frac{9}{4}\frac{\gamma_{\rm non\text{-}local}}{\tilde{\omega}_{\rm c}}(r\Omega)^2 - \frac{c^2}{6}\left[\left(1-\varepsilon_{\rm n}^2\right) + \frac{2}{7}\left(1-\varepsilon_{\rm t}^2\right)\left(1+\frac{5}{2}\frac{E_{\rm rot}}{E_{\rm kin}}\right)\right], \tag{18}$$

where $\tilde{\omega}_{\rm c} = \omega_{\rm c}/(\Omega\tau)$ is the normalized collision frequency. Note that the basic τ dependence of c in Fig. 2a can be understood by the local viscosity form in this equation.

The dependence of the factors $\gamma_{\rm local}/\tilde{\omega}_{\rm c}$ and $\gamma_{\rm non\text{-}local}/\tilde{\omega}_{\rm c}$ on $1-\varepsilon_{\rm t}$ and $\varepsilon_{\rm n}$ are examined in the same simulations of Fig. 2a using the method to obtain the viscosities described in Salo et al. (2001). The results are shown in Fig. 2b. When calculating the factors for the viscosities, we use the 'effective' collision frequency $\tilde{\omega}_{\rm c,eff} = \tilde{\omega}_{\rm c} \times (3\langle \mathbf{u}_{\rm n}^2\rangle)/(4c^2)$ instead of $\tilde{\omega}_{\rm c}$ itself, in order to avoid overestimation due to multiple hits, which take place between a same particle pair with very small time interval, and which have only a small effect on momentum transfer. Without multiple hits, $\langle \mathbf{u}_{\rm n}^2\rangle/c^2$ is expected to equal 4/3 from theoretical predictions (Hämeen-Anttila, 1983; see also Appendix A), and this is confirmed from our simulations with multilayer systems (the factor is also is shown in Fig. 2b). In Fig. 2b, $\gamma_{\rm local}/\tilde{\omega}_{\rm c,eff}$ is almost independent of $\varepsilon_{\rm t}$ but becomes larger with $\varepsilon_{\rm n}$, whereas $\gamma_{\rm non\text{-}local}/\tilde{\omega}_{\rm c,eff}$ clearly increases with both $1-\varepsilon_{\rm t}$ and $\varepsilon_{\rm n}$.

The physical meaning of the $\varepsilon_{\rm n}$ and $\varepsilon_{\rm t}$ dependence of the local viscosity is unclear (most likely they just reflect the modified properties of the steady-state depending on the amount of dissipation), but the dependence of the non-local viscosity is consistent with the theoretical prediction: the non-local viscosity is directly connected with collisional velocity changes in the direction of the orbital motion of the local coordinate (see Wisdom and Tremaine, 1988; Salo et al., 2001) and $\gamma_{\rm non\text{-}local}/\tilde{\omega}_{\rm c,eff}$ is expected to be proportional to $[(1+\varepsilon_{\rm n}) + c_t(1-\varepsilon_{\rm t})]$ (see Eq. (3)), where c_t is a numerical factor order of unity. Again, since the viscosity normalized by the collision frequency is an increasing function of $1-\varepsilon_{\rm t}$ and $\varepsilon_{\rm n}$ the velocity dispersion for larger $1-\varepsilon_{\rm t}$ and $\varepsilon_{\rm n}$ becomes larger if the energy dissipation $|\Delta E_{\rm kin}/E_{\rm kin}|$ is the same.

Three-body orbital integrations, which allow to examine ring viscous properties with a fixed velocity dispersion, will be another and more convenient way to discuss the dependence of the viscosity on $\varepsilon_{\rm t}$ and $\varepsilon_{\rm n}$ (Tanaka et al., 2003, Ohtsuki et al., in preparation).

3.1.2. *The critical value of $\varepsilon_{\rm n}$ for thermal instability*

If $\varepsilon_{\rm n}$ is larger than a critical value $\varepsilon_{\rm n,crit}(\varepsilon_{\rm t}, \tau)$, the velocity dispersion diverges because the viscous heating always exceeds the collisional damping. This condition was discussed by many previous works both for the non-friction case (e.g., Goldreich and Tremaine, 1978; Stewart et al., 1984; Salo, 1995; Ohtsuki, 1999; Schmidt et al., 1999) and for the friction case (Araki, 1988, 1991; Salo, 1987a). If the velocity dispersion is large enough, the non-local viscosity is negligible compared with the local viscosity. Thus the critical value can be obtained from Eq. (18) as

$$\varepsilon_{\rm n,crit}(\varepsilon_{\rm t}, \tau) = \left(1 - \frac{27}{2(1+\tau^2)}\frac{\gamma_{\rm local}}{\tilde{\omega}_{\rm c}} + \frac{2}{7}\left(1-\varepsilon_{\rm t}^2\right)\left(1+\frac{5}{2}\frac{E_{\rm rot}}{E_{\rm kin}}\right)\right)^{1/2}. \tag{19}$$

For non-friction particles Goldreich and Tremaine (1978) obtained the critical value is 0.627 for $\tau = 0$, which gives $\gamma_{\rm local}/\tilde{\omega}_{\rm c} = 0.045$. Assuming that this value is fixed, we plot $\varepsilon_{\rm n,crit}$ as a function of $\varepsilon_{\rm t}$ for $\tau = 0.05$ and 0.40 in Fig. 3.

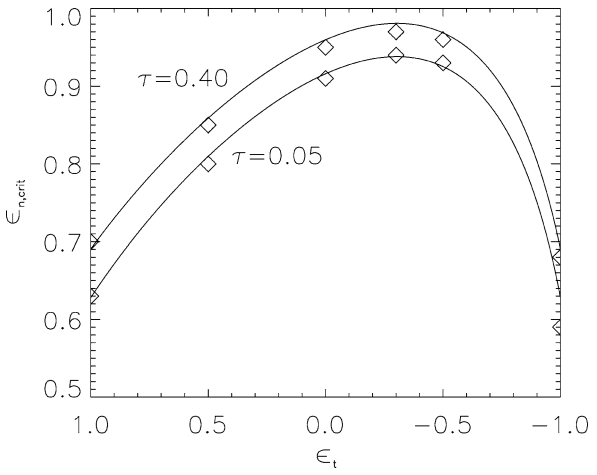

Fig. 3. The critical value of the coefficient of normal restitution as a function of $\varepsilon_{\rm t}$ for $\tau = 0.05$ and 0.40. Solid curves show analytic solutions which assume the Goldreich and Tremaine value $\varepsilon_{\rm n,crit} = 0.627$ for $\varepsilon_{\rm t} = 1.0$ and $\tau \to 0$. Diamonds denote the maximum $\varepsilon_{\rm n}$'s for which the simulated velocity dispersion remains below 25 $r\Omega$, with the accuracy up to a second decimal place. The actual critical value of $\varepsilon_{\rm n}$ is slightly higher (by about 0.01).

In order to confirm the validity of these curves, in other words, to check how closely $\gamma_{\rm local}/\tilde{\omega}_{\rm c}$ remains constant for different $\varepsilon_{\rm t}$ and τ in the case $c \gg r\Omega$, we performed local simulations to obtain $\varepsilon_{\rm n,crit}$ with varying $\varepsilon_{\rm n}$. However, this leads to practical difficulties, since the validity of the local simulation method becomes questionable when the excursions of particles become comparable to the simulation box size (the velocity dispersion attains larger and larger steady-state values as $\varepsilon_{\rm n}$ approaches $\varepsilon_{\rm n,crit}$). Therefore, instead of trying to obtain the precise values of $\varepsilon_{\rm n,crit}$, we search $\varepsilon_{\rm n}$ which gives a velocity dispersion of about $25r\Omega$, as done in Schmidt et al. (1999). This value should be large enough to neglect the contribution from the non-local viscosity. The actual $\varepsilon_{\rm n,crit}$ would then be slightly larger than these values obtained in simulations. We find that Eq. (19) fits surprisingly well the values obtained in simulations both for $\tau = 0.05$ and 0.40 (within 0.01 except for the case of $\varepsilon_{\rm t} = -1.0$ and $\tau = 0.05$). This result suggests that $\gamma_{\rm local}/\tilde{\omega}_{\rm c}$ can be treated as a constant for multilayer rings.

We also find that the obtained $\varepsilon_{\rm n,crit}$ for $\tau = 0.05$ is well consistent with those obtained by Araki (1988) for $\tau \to 0.0$ (the difference caused by slightly different τ of 0.05 is quite small) rather than Araki (1991); the latter one includes the effect of

the volume filling factor while the former one neglected it (see Fig. 3 of Araki, 1991). This seems to suggest that the treatment of the filling factor in Araki (1991) is not very accurate for low filling factors.

By using a velocity-dependent ε_n instead of varying ε_n in different simulations, we can also obtain an approximate $\varepsilon_{n,crit}$: in this case the system attains a steady-state where the average dissipation in impacts balances the viscous gain. Therefore, the weighted average value $\langle \varepsilon_n \mathbf{u}_n^2 \rangle / \langle \mathbf{u}_n^2 \rangle$ gives a quite similar value from the theoretical prediction. This is true as long as the equilibrium velocity dispersion is large, whereas a very inelastic velocity dependent ε_n gives a smaller $\langle \varepsilon_n \mathbf{u}_n^2 \rangle / \langle \mathbf{u}_n^2 \rangle$, in order to compensate for the energy input by the non-local viscosity (Salo, 1987a, 2000).

3.1.3. *Closely packed ring*

Now let us return to the behavior of the most closely packed case in Fig. 2 (with $\varepsilon_n = 0.1$ and $\tau = 1.0$). In such closely packed rings, collisions are no longer random but multiple collisions occur for a same particle pair with very small time intervals, or one particle may hit other two particles alternatively. The spin velocity changes take place in the same sense in all these subsequent multiple collisions, so that spin velocities are enhanced in comparison to theoretical predictions assuming random impact directions. However, when using the force model instead of the instantaneous model, the enhancement is strongly suppressed (Fig. 4). The reason for this is that during multiple collisions the normal component of impact velocity remains usually small, so that the tangential force is limited in the force model. In this respect, the force model appears to be more realistic.

3.1.4. *Mean spin rate*

The planar components of mean spin rate become zero due to the symmetry in the vertical (z) direction, but $\langle \omega_z \rangle$ is not canceled out. In theoretical predictions, $\langle \omega_z \rangle$ is estimated to approach about 0.3–0.4Ω (Salo, 1987a; Araki, 1991; Ohtsuki, 2004a) and to be almost independent of ε_n and ε_t. Our results are more or less the same (Fig. 2a). However, $\langle \omega_z \rangle$ for the most closely packed case is a little bit smaller. In fact, this suggests that during multiple collisions mentioned above, the mutual rotation for a colliding pair in the retrograde direction is more preferable than the prograde direction, since the Coriolis force acts as an attractive force for a retrograde rotation. Since a collision in a retrograde direction reduces ω_z, the average value becomes smaller. In Fig. 4, the decrease of $\langle \omega_z \rangle$ with τ can be clearly seen even for the more elastic case ($\varepsilon_n = 0.5$) or for the force model, because multiple collisions happen more often for larger τ.

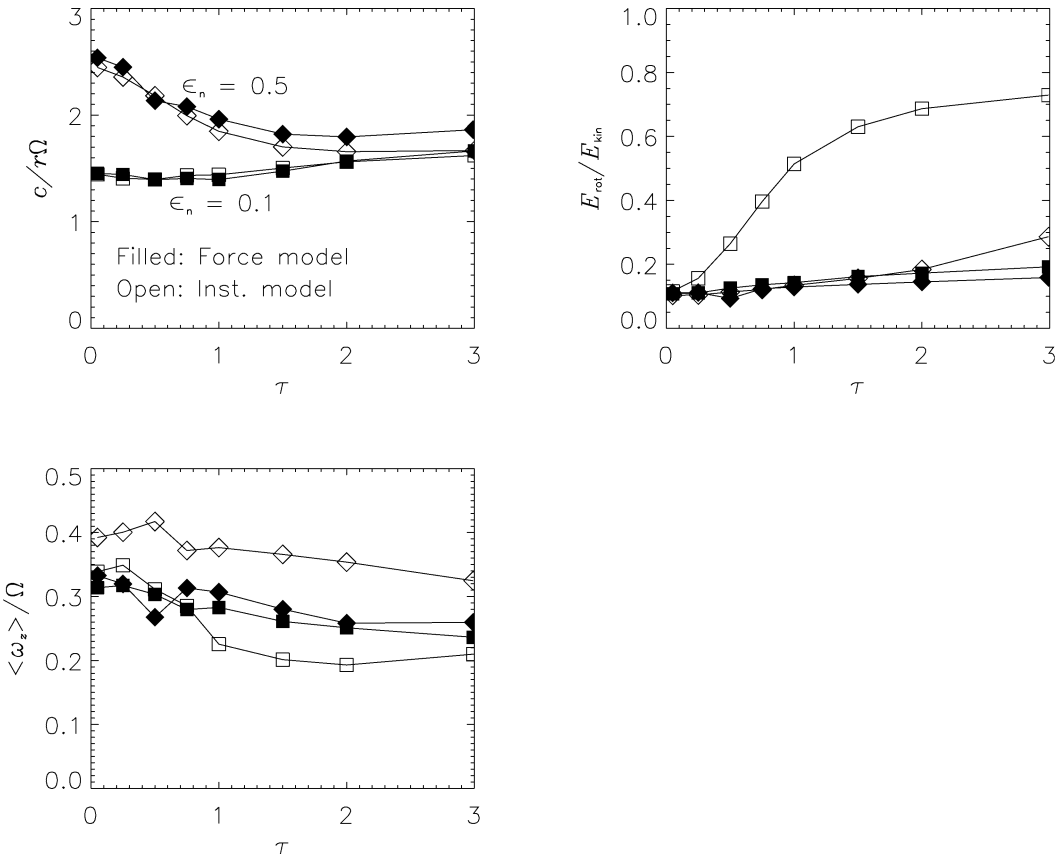

Fig. 4. Comparison of the instantaneous impact model (open symbols) and the force model (filled symbols) for $\varepsilon_t = 0.5$. The velocity dispersion c, the energy ratio E_{rot}/E_{kin}, and the z-component of the mean spin $\langle \omega_z \rangle$ are shown as functions of optical depth τ, for $\varepsilon_n = 0.1$ and 0.5 (squares and diamonds, respectively). The spin dispersion obtained by the instantaneous impact model is greatly enhanced for closely packed systems (i.e., cases with high τ and small ε_n).

3.2. Self-gravitating identical particles

Once we include the self-gravity of particles, the velocity dispersion is enhanced by mutual gravitational scatterings. Further, gravitational wakes or/and oscillations caused by viscous overstability add large systematic motions to the random velocities for optically thick rings (Salo, 1995; Daisaka and Ida, 1999; Salo et al., 2001). Though the dispersion of spin velocity is enhanced for the self-gravity case, the large systematic motions do not have much extra effect on the spin dispersion.

The strength of mutual gravity force of each ring particle pair is characterized by the ratio of the sum of the particle radii to the Hill radius (Ohtsuki, 1993): $r_\mathrm{p} = (r_1 + r_2)/r_\mathrm{Hill}$ with $r_\mathrm{Hill} = a(m_1 + m_2)^{1/3}/(3M_*)^{1/3}$, where a is the semimajor axis of the particles, and M_* is the mass of the planet. For Saturn's rings

$$r_\mathrm{p} = 0.77\left(\frac{\rho}{900\ \mathrm{kg\,m^{-3}}}\right)^{-1/3}\left(\frac{a}{10^8\ \mathrm{m}}\right)^{-1}\frac{1+\mu^{1/3}}{(1+\mu)^{1/3}}, \qquad (20)$$

where ρ is the density of the particles and $\mu = m_2/m_1$. The self-gravitational force gets stronger relative to the tidal force with decreasing r_p, and mutual accretion becomes possible for $r_\mathrm{p} < 1$. In most of the self-gravitating simulations, we use $a = 10^8$ m and $\rho = 900\ \mathrm{kg\,m^{-3}}$ as standard values ($r_\mathrm{p} = 1.22$ for identical particles). However, note that the same ring structure is obtained for the same r_p value: for example, $a = 1.26\times10^8$ m and $\rho = 450\ \mathrm{kg\,m^{-3}}$.

Fig. 5 shows the equilibrium properties for self-gravitating rings with identical particles as functions of ε_t. The velocity dispersion for optically thin rings is in principle of the order of the escape velocity of a particle $v_\mathrm{esc} = \sqrt{2Gm/r}$. In terms of $r\Omega$, this gives

$$\frac{v_\mathrm{esc}}{r\Omega} = 3.64\left(\frac{\rho}{900\ \mathrm{kg\,m^{-3}}}\right)^{0.5}\left(\frac{a}{100{,}000\ \mathrm{km}}\right)^{1.5}. \qquad (21)$$

On the other hand, the velocity dispersion for optically thick rings is much larger than the escape velocity. Previous studies suggest that when wakes are made by near-gravitational instability the Toomre parameter Q is always about 1–2 (Salo, 1995; Daisaka and Ida, 1999; Salo et al., 2001), where Q is defined as (Toomre, 1964)

$$Q = \frac{\kappa c_\mathrm{r}}{3.36G\Sigma}, \qquad (22)$$

where the epicyclic frequency κ equals Ω in a Keplerian velocity field and c_r stands for the radial velocity dispersion. We find that $c_\theta \simeq 0.5c_\mathrm{r}$ is always satisfied, where c_θ stands for the velocity dispersion in the orbital direction, whereas the velocity dispersion in the perpendicular direction c_z to the orbital plane is smaller than those of planar components. Therefore, using Eq. (22) and considering only the planar components, the typical velocity dispersion for optically thick rings with gravi-

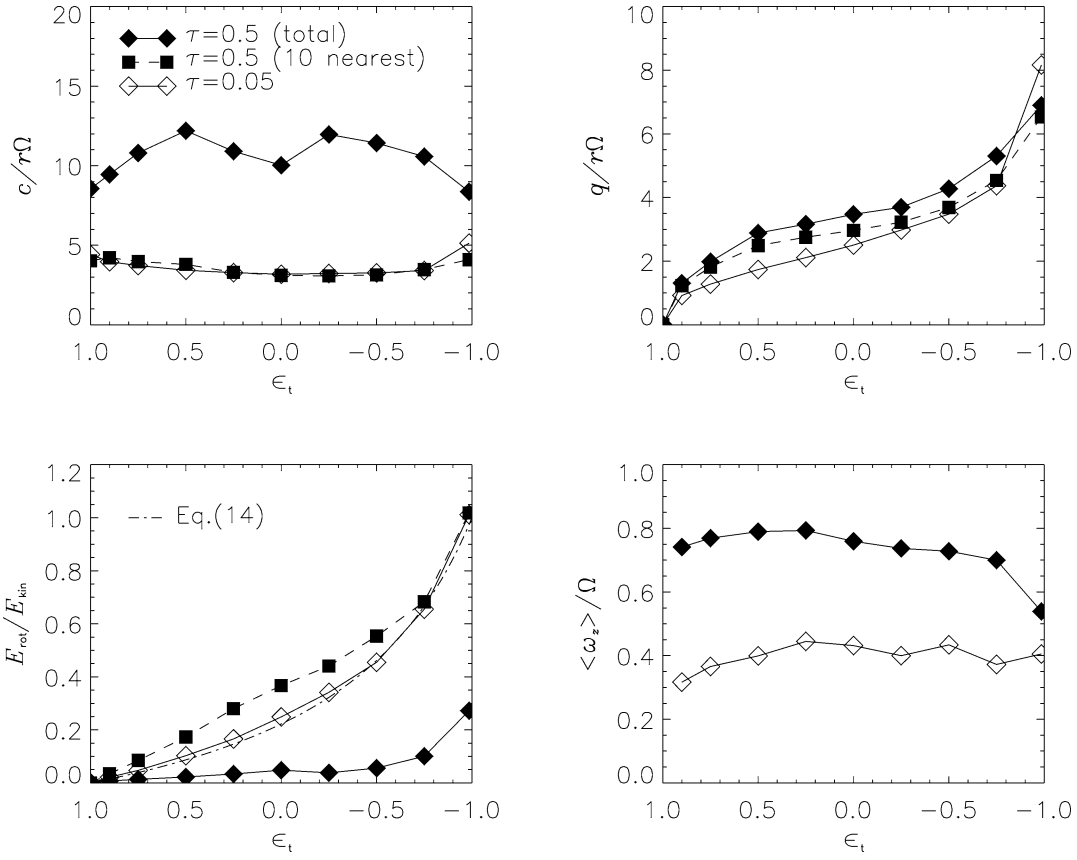

Fig. 5. The same as Fig. 2a but for rings with self-gravitating particles. The cases for $\tau = 0.05$ (open diamond) and 0.5 (filled diamond) are shown, respectively, with $\varepsilon_\mathrm{n} = 0.5$, $a = 100{,}000$ km, and $\rho = 900\ \mathrm{kg\,m^{-3}}$. For $\tau = 0.5$, the local dispersions of velocity and spin velocity are calculated using the 10 nearest neighboring particles; these are denoted by filled squares. For $\tau = 0.05$ there is no difference between local and total values.

tational wakes is given by

$$\frac{c_{\rm wake}}{r\Omega} = 7.94\left(\frac{\rho}{900\ {\rm kg\,m^{-3}}}\right)\left(\frac{a}{100{,}000\ {\rm km}}\right)^3\left(\frac{\tau}{0.5}\right), \qquad (23)$$

where we adopt $Q = 2$. The velocity dispersion for $\tau = 0.5$ in Fig. 5 is similar to the expected value.

It should be noted that c for $\tau = 0.5$ becomes larger with energy dissipation rate (with $\varepsilon_{\rm t}$ decreases from unity), which is opposite to the case of $\tau = 0.05$. Since the tendency of grouping of particles increases for larger energy dissipation, the effect of self-gravity is enhanced for rings with large τ (the tendency in Fig. 5 may not be clear due to our short simulation period $\sim 15T_{\rm K}$ and to temporal fluctuation of velocity dispersion, although this period is long enough to obtain the equilibrium local velocity dispersion as we will see below). The same effect can be obtained by reducing $\varepsilon_{\rm n}$ (Salo, 1995).

The self-gravity enhances the spin velocity dispersion compared with non-self-gravitating cases. This is because impact velocity is increased due to enhanced velocity dispersion and due to the acceleration before collisions. However, in contrast to the behavior of velocity dispersion, the dispersion of spin velocity is not strongly dependent on the optical depth. This suggests that the mutual impact velocity is only weakly dependent on the optical depth of rings. In order to confirm this fact, we calculated the local dispersions of translational and spin velocities using the 10 nearest neighbors, as done by Salo (1995) and Daisaka and Ida (1999). The results are shown by dashed curves in Fig. 5. We find that the local velocity dispersion for $\tau = 0.5$ is surprisingly consistent with the (total) velocity dispersion for $\tau = 0.05$. It means that while the mutual relative velocity between different wakes is much larger than the escape velocity of a particle, in each wake the relative velocity of particles always remain close to the escape velocity. The local spin velocity dispersion is also slightly smaller than the total dispersion because impacts tend to align the spin axes of colliding pairs. However, the difference is not very significant.

The energy ratio $E_{\rm rot}/E_{\rm kin}$ for optically thin cases is well consistent with the analytic prediction given by Eq. (14). For larger optical depth cases, $E_{\rm rot}/E_{\rm kin}$ is much smaller than the analytic prediction due to enhanced velocity dispersion. However, if we again use the local velocity dispersions instead of the total dispersions, similar agreement is obtained as for the optically thin cases. We only show the case of $\varepsilon_{\rm n} = 0.5$ in Fig. 5. On the other hand, for $\varepsilon_{\rm n} = 0.1$ the $E_{\rm rot}/E_{\rm kin}$ obtained by using local dispersions for $\tau = 0.5$ is significantly enhanced compared to the analytic prediction. The mechanism of this enhancement is exactly the same as that explained in the context of the non-gravitating case with $\tau = 1.0$ and $\varepsilon_{\rm n} = 0.1$ (see Section 3.1).

The z component of mean spin rate $\langle\omega_z\rangle$ for the optically thick case is much larger than in the optically thin case. This enhancement is related to gravitational wakes (details will be discussed in connection to Fig. 7). For $\tau = 0.5$, there is a strong reduction in $\langle\omega_z\rangle$ for $\varepsilon_{\rm t} = -1.0$ (Fig. 5), in which case the local velocity dispersion remains so large that global collective motions are less enhanced.

Fig. 6 shows dependences of the dispersions of velocity and spin velocity on the optical depth τ and the semimajor axis a, obtained by using the force model with $k_{\rm f} = 0.1$. We use a fixed value $a = 100{,}000$ km for the τ dependence and a fixed value $\tau = 0.5$ for the a dependence. In the left frame of Fig. 6 the total velocity dispersion increases significantly with τ, whereas the local velocity dispersion remains comparable to the escape velocity, as we explained in connection to Fig. 5. As a result, the spin velocity dispersion is also the order of the escape velocity.

In the right frame for the a dependence, we normalize the dispersions by the escape velocity $v_{\rm esc}$ instead of $r\Omega$, in order to clarify the difference between the total and local dispersions more clearly. The dispersions decrease with increasing distance for small a, whereas opposite trend appears for larger a. Impacts in a differentially rotating system always maintain a certain minimum velocity dispersion $\sim 2r\Omega$ (e.g., Salo, 1995; Ohtsuki, 1999), which is larger than $v_{\rm esc}$ and $c_{\rm wake}$ (Eqs. (21) and (23)) for small a. Since Ω decreases with a the velocity dispersions decreases for small a. On the other hand, the self-gravity determines the dispersions for larger a. For optically thick cases like $\tau = 0.5$ in Fig. 6, the total velocity dispersion follows $c_{\rm wake}$, which increases strongly with a (see Eq. (23)). Interestingly, the local velocity dispersion and the spin dispersion (both local and total) also increase with a, although the magnitude of the increase is much smaller than that for the total velocity dispersion. This suggests that local motion inside wakes is not completely independent of the relative motions of the wakes. In a single gravitational wake, collision velocity might be very close to the escape velocity. However, wakes also collide with each other, especially in the case of strong self-gravity (large a), where the wakes become increasingly irregular. That is probably the reason why the local velocity dispersion exceeds the escape velocity for larger a (we confirmed that enhancement of the local velocity dispersion in larger a cannot be seen for small τ cases). Altogether, $E_{\rm rot}/E_{\rm kin}$ obtained by using local dispersions is quite insensitive to τ and a, and is close to the analytical prediction.

Fig. 7 shows dependences of the z-components of mean spin rate $\langle\omega_z\rangle$ on optical depth τ and semimajor axis a, obtained in the simulations of Fig. 6. As one can see, $\langle\omega_z\rangle$ increases with τ and a. This enhancement was already found by Salo (1995) and Ohtsuki and Toyama (2005), but the mechanics has not been clarified. Morishima and Salo (2004a) suggested enhancement of $\langle\omega_z\rangle$ in terms of sliding of particles on large clumps temporally made in wake structures. However, it is expected that sliding on such a rough surface may not be efficient as compared with that on a spherical surface assumed in Morishima and Salo (2004a). Here we propose another mechanism to enhance $\langle\omega_z\rangle$. In gravitational wakes, particles move coherently and collectively and the local shear rate $-{\rm d}v_y/{\rm d}x$ is reduced compared to the Keplerian shear rate, where v_y denotes the velocity of the guiding center of the particle motion in the orbital direction and x points the radial direction. Because impacts with large shear velocities bring small or negative angular momentum to colliding particles and vise versa, $\langle\omega_z\rangle$ in fact increases with decreasing the local shear rate. This is also suggested by the analytic solution of $\langle\omega_z\rangle$, derived with neglecting the self-gravity,

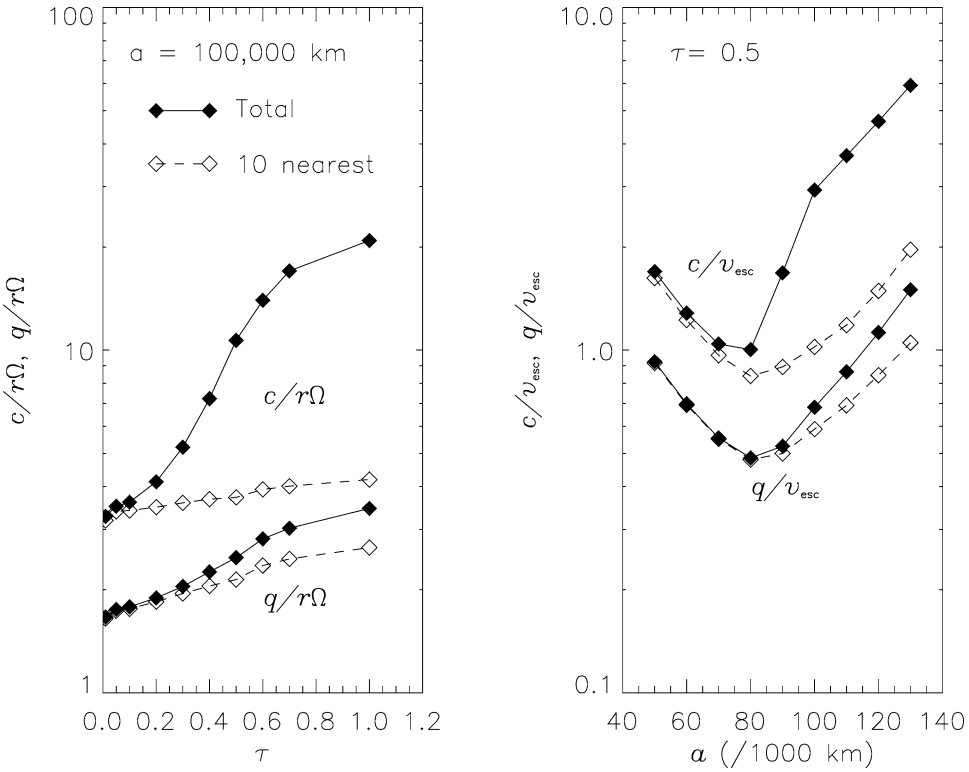

Fig. 6. Dependence of the velocity dispersion c and the spin velocity dispersion q on the optical depth τ (left frame), and on the saturnocentric distance a (right frame). The force model is used with $k_f = 0.1$, $\varepsilon_n = 0.5$, and $\rho = 900\ \mathrm{kg\,m^{-3}}$. The local dispersions obtained by using the 10 nearest neighboring particles are shown by open diamond symbols. In the left frame $a = 100{,}000$ km is assumed and the dispersions are normalized by $r\Omega$. In the right frame $\tau = 0.5$ is assumed and the dispersions are normalized by the escape velocity v_{esc}.

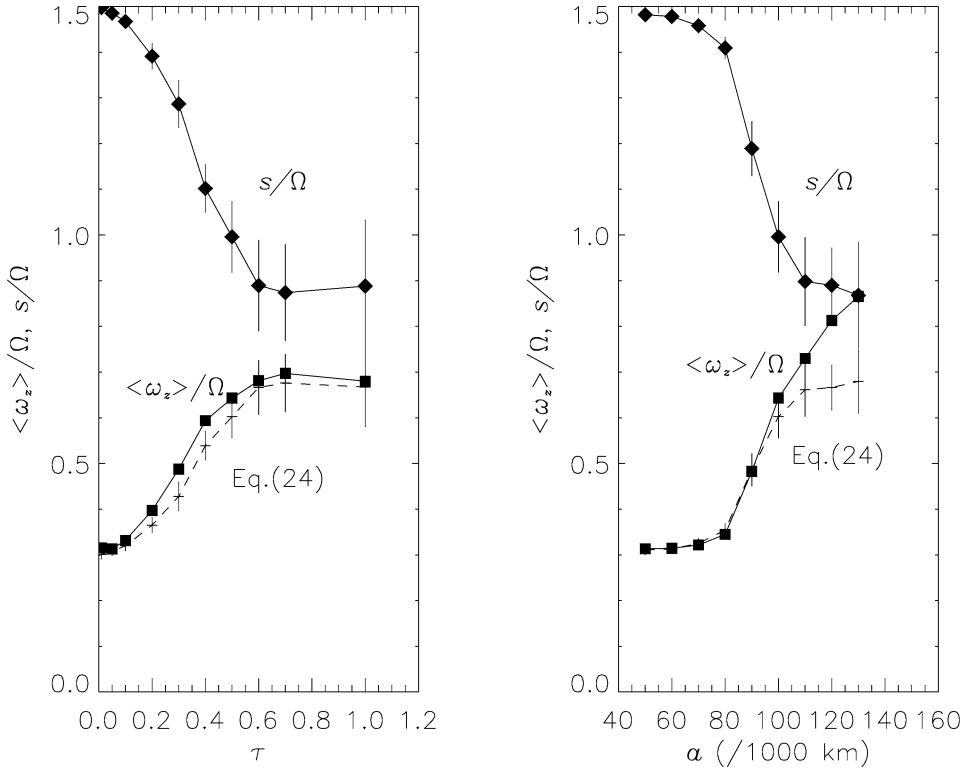

Fig. 7. Dependence of the z-component of the mean spin $\langle\omega_z\rangle$ (square symbols) on the optical depth τ (left frame), and on the distance a (right frame). The simulation parameters are the same as those of Fig. 6. The local shear rate s (diamond symbols) obtained by using the 10 nearest neighboring particles, and the analytic prediction of the z-component of the mean spin (dashed curves) given by Eq. (24) are also shown.

as a function of the local shear rate (Salo, 1987a, see also Appendix B):

$$\langle\omega_z\rangle_{\rm ana} = \frac{6}{5}\left(1-\frac{s}{2}\right)\Omega, \tag{24}$$

where $s = -(1/\Omega)\,\mathrm{d}v_y/\mathrm{d}x$ denotes the normalized shear rate. For the case of the Keplerian shear rate ($s = 3/2$), this equation gives $\langle\omega_z\rangle = 0.3\Omega$.

We have also calculated the local shear rate in simulations, using again the 10 nearest neighbors around each particle, like we did in order to estimate the local velocity dispersion. In Fig. 7 we over-plot the local shear rate s and $\langle\omega_z\rangle_{\rm ana}$ obtained by substituting s into Eq. (24). We find excellent agreement between $\langle\omega_z\rangle$ and $\langle\omega_z\rangle_{\rm ana}$ except for large a. For large a, transient large clumps are formed, which could modify the mean spin velocity. In the limit of large a all particles accrete to clumps, and the spins of these clumps are almost synchronous ($\langle\omega_z\rangle = \Omega$) thus s becomes zero (Karjalainen and Salo, 2004). Since the above analytic equation gives $\langle\omega_z\rangle = 1.2\Omega$ for $s = 0$, there is clearly some shortcomings for the analytic solution for small s near 0. Except for this extreme case, the enhancement of $\langle\omega_z\rangle$ seems to be explained quite naturally by the reduced local shear rate.

Closely packed rings with optical depth $\tau > 1$ can also exhibit spontaneous viscous oscillatory instability, termed viscous overstability (e.g., Schmit and Tscharnuter, 1999; Spahn et al., 2000; Salo et al., 2001; Schmidt et al., 2001; Daisaka et al., 2001; Schmidt and Salo, 2003). Axisymmetric oscillations are formed by this instability and can co-exist with the non-axisymmetric wakes formed by near-gravitational instability. With decreasing self-gravity, for example by reducing the particles' internal density ρ for a fixed a, the axisymmetric oscillations become more dominant in comparison to wakes. Fig. 8 shows an example of temporal evolution of dispersions of translational and spin velocities when the overstability is induced. The velocity dispersion increases with time whereas the local velocity dispersion as well as the spin velocity dispersion are only weakly affected by the large systematic motions related to overstability. We also find that the onset of overstability becomes slightly easier with stronger friction, since this leads to increased dissipation rate. However, the dependence of the instability on $\varepsilon_{\rm n}$ and size distribution seems much more important than that on $\varepsilon_{\rm t}$.

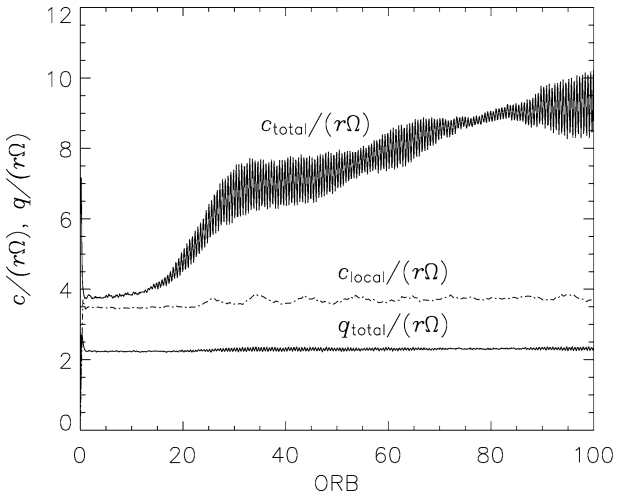

Fig. 8. Evolution of translational and spin velocity dispersions (solid curves). Oscillatory instability (overstability) enhances translational velocity dispersion. The local dispersion obtained by using the 10 nearest neighboring particles is shown by the dot-dashed curve. The simulation parameters are $\tau = 1.39$, $r = 2$ m, $\rho = 225\ \mathrm{kg\,m^{-3}}$, $N = 15{,}000$, $k_{\rm f} = 0.1$. These are almost the same as those used in the bottom row of Fig. 1 in Salo et al. (2001).

Altogether, the spin velocity dispersion seems to be only slightly affected by large scale systematic motions, either related to gravitational wakes or viscous overstability. This suggests that the same might be true also for the density waves induced by satellite resonances.

3.3. Power law size distribution

So far, we have discussed the properties of rings with identical particles. As long as we consider only identical particles, the spin frequencies are of the order of the orbital frequency. The situation turns out to be drastically different if we allow for the particle size distribution.

We adopt a power law distribution of particles with the upper and lower cut-off sizes as

$$\frac{\mathrm{d}N}{\mathrm{d}r} \propto r^{-q_{\rm s}}, \quad r_{\rm min} < r < r_{\rm max}. \tag{25}$$

According to the voyager I radio occultation measurements (Marouf et al., 1983), $q_{\rm s} \simeq 3$ and $r_{\rm max}/r_{\rm min} = 500$ with $r_{\rm min} = 1$ cm. The recent analysis by French and Nicholson (2000) suggests similar values $q_{\rm s}$, but the range of particle size is different in each ring: $r_{\rm max}/r_{\rm min} = 1000$ with $r_{\rm min} = 1$ cm for the C ring whereas $r_{\rm max}/r_{\rm min} \simeq 70$ with $r_{\rm min} = 30$ cm for the A and B rings. In either cases, these widths of the size distribution are still too large for direct N-body simulations and we need to truncate the size distribution to a shorter width (see Appendix C for the required number of particles in simulations). Therefore, we first conduct non-self-gravitating simulations with a rather large $r_{\rm max}/r_{\rm min}$ (up to 100) and examine the dependence of various steady-state quantities on the width of size distribution. Secondly, we conduct self-gravitating simulations with a rather small $r_{\rm max}/r_{\rm min}(=10)$, and based on the non-self-gravitating simulations speculate what might be the behavior of the self-gravitating rings with realistic larger $r_{\rm max}/r_{\rm min}$.

Fig. 9 shows the dependence of ring steady-state quantities on width of size distribution, for a non-self-gravitating case with $q_{\rm s} = 3$, $\tau = 1$, and $\varepsilon_{\rm n} = \varepsilon_{\rm t} = 0.5$, obtained by using the instantaneous impact model. The difference between the largest and smallest particles in the velocity dispersion is quite small as compared with that in their sizes, and increases only slightly with the width of the size distribution. The equipartition of the kinetic energy, $0.5mc^2$, between larger and smaller particles is not achieved. This is essentially due to the larger energy dissipation rate for smaller particles with larger velocities (Salo, 1987a, 1987b, 1991, 1992a). Since impact velocities are not so different with different size of particles, the dependence of the spin velocity dispersion on the particle size is quite small as well. This means that the spin frequency (the spin velocity

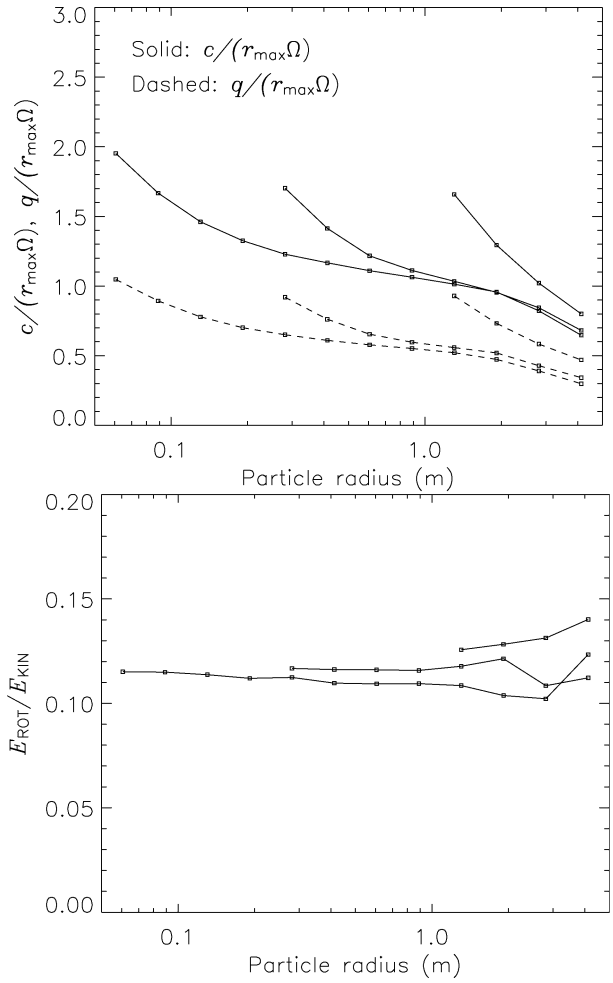

Fig. 9. Dependences of the dispersions of velocity and spin velocity (solid and dashed curves in upper frame, respectively) and the spin/kinetic energy ratio (lower frame) on the width of size distribution for non-self-gravitating particles. The power law index $q_s = 3$ and the maximum size of particles $r_{max} = 5$ m are assumed. Three different cases of the minimum size of particles $r_{min} = 0.050$, 0.232, 1.077 m with the fixed total optical depth $\tau = 1.0$ are shown. The instantaneous model is used with $\varepsilon_n = \varepsilon_t = 0.5$.

divided by the particle radius) is roughly proportional to $1/r$. Ohtsuki (2005) obtains a similar size-dependence of the spin frequency for optically low rings. These results are very important for the interpretation of thermal infrared emission of rings (see the next section for more discussion).

The energy ratio E_{rot}/E_{kin} in Fig. 9 is almost independent of the particle size and close to the case of identical particles (0.134 for $\tau = 1.0$ and $\varepsilon_n = \varepsilon_t = 0.5$ in Fig. 2a). However, the ratio is slightly enhanced for the largest particles and this looks opposite to the theoretical prediction (Salo, 1987a). In fact, smaller particles make multiple collisions on the largest particles, resulting in the slight enhancement of the energy ratio for the largest particles. This is basically the same mechanism which was discussed in Section 3.1 for closely packed rings.

Fig. 10 shows the self-gravitating ring quantities for $q_s = 3$, $\tau = 0.5$, $r_{max}/r_{min} = 10$, and $r_{max} = 5$ m with different a. This size distribution gives the effective particle radius $r_{eff} = 3\Sigma/(4\rho\tau) = 1.95$ m. Since the typical velocity dispersion of gravity wakes is proportional to Σ (see Eq. (23)), it is convenient to normalize the velocity dispersion by $r_{eff}\Omega$ when comparing with the simulations of identical particles with the same τ and ρ. We find that the behavior of the largest particles is quite similar to that in the corresponding identical particle case for all the quantities shown in Fig. 10. On the other hand, the velocity dispersion of the smallest particles is about doubled compared to that of the largest particles. This is similar to the non-self-gravitating case, although the velocity dispersions themselves are now much larger than in the non-self-gravitating case. These results suggest that the largest particles are permanently stuck to the wakes (or wakes form predominantly around them), while the smaller particles move more freely between the wakes (see also Salo et al., 2004).

The dependence of the spin velocity dispersion on the particle size is somewhat stronger than that of the velocity dispersion: the spin velocity dispersion for the smallest particles is about 3–4 times that of the largest particles' values. As a result, in contrast to the non-self-gravitating case E_{rot}/E_{kin} decreases with particle size. This dependence can be explained as follows. For $q_s = 3$ the total mass is dominated by the largest particles even though the contribution to the optical depth from each size of particles divided logarithmically is the same. Therefore, the spin state of the largest particles is determined by mutual collisions between the largest particles themselves, since the momentum given by smaller particles is insignificant. The relative velocity of largest particles, which are stuck to wakes, is close to their mutual escape velocity v_{esc} rather than the global dispersion c_{wake} (Eq. (23)); this is similar to what was seen in the identical particle case (Section 3.2). Therefore, the spin dispersion of the largest particles is roughly given by $v_{esc} \times \sqrt{5(1-\varepsilon_t)/(9+5\varepsilon_t)}$ (see Eq. (14) for the factor). On the other hand, the spin state of the small particles is affected by collisions with all other particles. The impact velocity of smallest particles, which move between wakes, are similar to c_{wake}. Hence, the spin dispersion of the smaller particles becomes also of the order of c_{wake}.

It should be noted that the value of E_{rot}/E_{kin} for the smallest particles is rather close to that of the non-self-gravitating case, since their motions are random unlike large particles in wakes. It can be expected that the value of E_{rot}/E_{kin} for smaller particles will reach the same asymptotic value as in the non-self-gravitating case if the size distribution is sufficiently extended. Therefore, we expect that the rather steep dependence of q on the particle size seen in simulation of Fig. 10 is limited to the large particles, whereas the distribution is expected to be less steep for the small particles if realistic wide distributions are studied.

In the present paper, we showed size distribution cases only for optically thick rings. For the case of small optical depth, in fact, E_{rot}/E_{kin} decreases with size near the large size end, as well as optically thick cases. Recent studies by Ohtsuki (2005) and Ohtsuki and Toyama (2005) based on three-body formulation and N-body simulations, respectively, also pointed out that spin frequency is approximately proportional to $1/r$ (corresponding to a constant q), but size-dependence of spin frequency near the large size end becomes steeper for optically thin cases. However, the mechanism causing the steeper size-

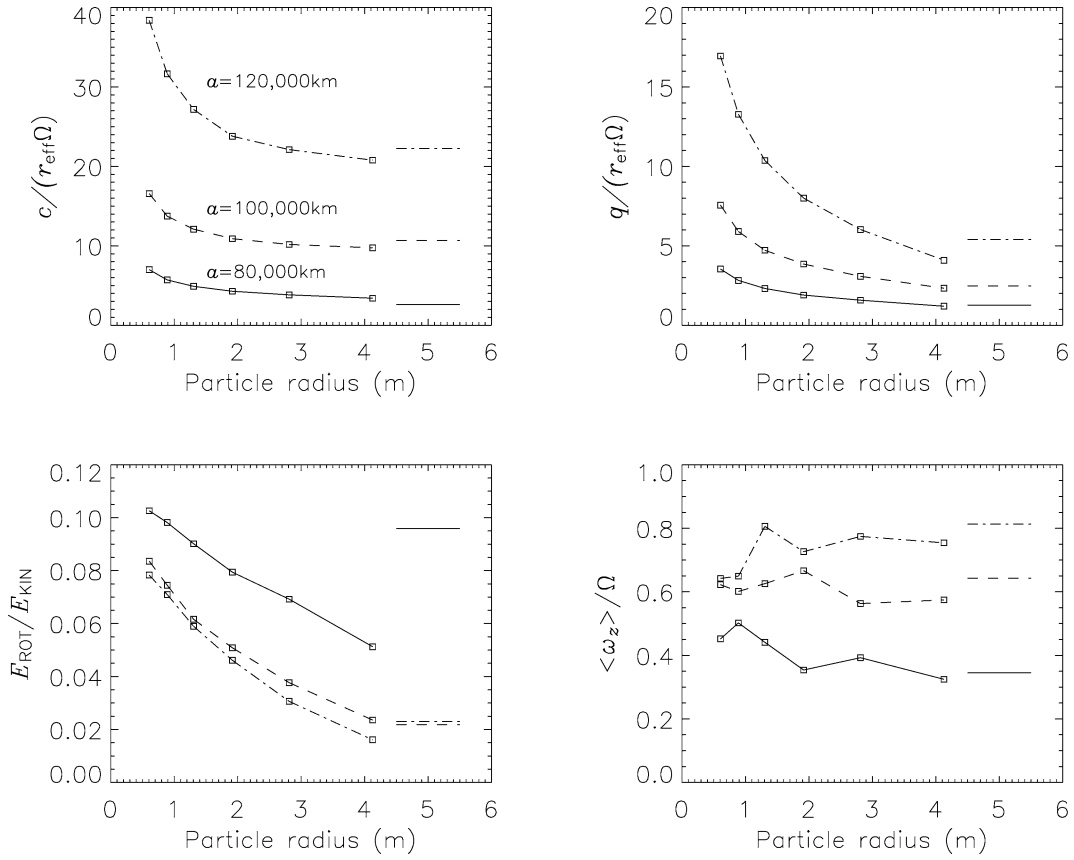

Fig. 10. The equilibrium state of rings of self-gravitating particles with size distribution for $\tau = 0.5$, $q_s = 3$, $r_{min} = 50$ cm, $r_{max} = 5$ m, and $r_{eff} = 3\Sigma/(4\rho\tau) = 1.95$ m. The results for three different distances $a = 80{,}000$, 100,000, and 120,000 km (solid, dashed, dot-dashed curves) are shown. The force model is used with $k_f = 0.1$, $\varepsilon_n = 0.5$, and $\rho = 900\,\mathrm{kg\,m^{-3}}$. For comparison, the horizontal lines show the corresponding values in the cases with identical particles (from Figs. 6 and 7).

dependence in the large size end for optically thin rings must be different from that for optically thick self-gravitating rings: we have explained the latter mechanism in the above, and more explicit physical explanations for the former mechanism will be given in future works (e.g., Ohtsuki, in preparation).

In Fig. 10, the mean spin rate $\langle\omega_z\rangle$ increases with the strength of self-gravity (larger a) for all the sizes of particles. The enhancement of the largest particles is caused by the same reason as we explained for identical particle cases in Section 3.2. On the other hand, $\langle\omega_z\rangle$ of smaller particles is enhanced by accretion or sliding on the largest particles. When a small particle accretes on a large particle, their velocity difference $\mathbf{u}$ (Eq. (1)) and relative velocity v_r tend to vanish due to the dissipation. As a result, we obtain $\omega_{1,z} \simeq r_1/r_2(\Omega - \omega_{2,z}) + \Omega$, where $\omega_{1,z}$ and $\omega_{2,z}$ are z-components of spin rates for small and large particles, respectively, and this suggests that spin rates of small particles' on large particles tend to be larger than Ω, since $\langle\omega_{2,z}\rangle < \Omega$ (see also Morishima and Salo, 2004a). Since the effect of accretion or sliding becomes more important with larger a, the averaged $\langle\omega_z\rangle$ for smaller particles is more enhanced. This mechanism may not be very clear in the case of a narrow size distribution like in Fig. 10, but would be more pronounced for a wider size distribution. In the simulations of Richardson (1994), the enhance of $\langle\omega_z\rangle$ for smaller particles is not seen. This is probably because his simulation time is too short. The time scale to acquire the equilibrium value of $\langle\omega_z\rangle$ is much longer than those for other quantities (e.g., Salo, 1987b).

The effect of the size distribution on the dynamical behavior of rings seems not so significant when gravitational wakes form, since the velocity dispersion of the largest particles is almost the same as that of identical particles, as we explained above. This is probably because of several competing effects: some of the smaller particles fill the voids in the wakes and thus enhance the strength of gravity (Karjalainen and Salo, 2004), whereas other fast moving small particles stir wake motions and tend to reduce their strength.

We also confirmed that the total viscosity (the sum of the local, non-local, and gravitational viscosities) normalized by $r_{eff}^2\Omega$ is almost independent of the width of size distribution. When gravitational wakes form, the gravitational viscosity and the local viscosity are almost equal, and the non-local viscosity becomes negligible (Daisaka et al., 2001). Salo et al. (2004) reported that the wake angle with respect to the direction of the orbital motion becomes steeper and the typical wake tangential length becomes shorter for size distribution case as compared with the identical particle case. While the steeper angle enhances the angular momentum transfer by the self-gravity and thus the gravitational viscosity, the shorter wake length decrease it. It seems that the effects more or less compensate and the resulting viscosity is almost independent of the size

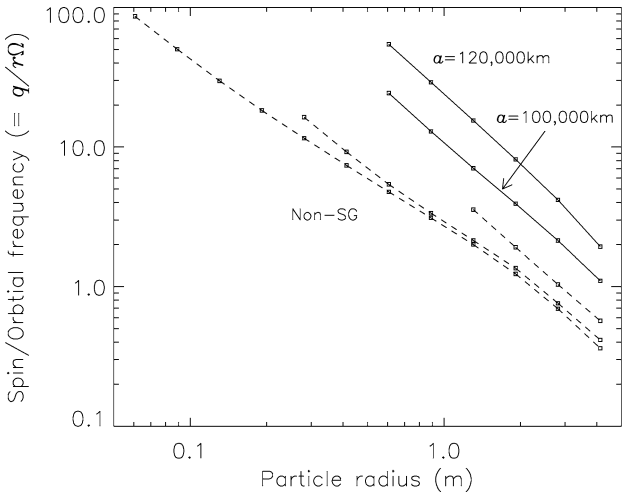

Fig. 11. Dependence of spin frequency q/r on particle size. Both cases with (solid curves) and without (dashed curves) the self-gravity are shown. The simulation results for non-self-gravitating case are from Fig. 9 whereas those for self-gravitating case are from Fig. 10.

distribution. On the other hand, the formation of oscillations by viscous overstability is clearly suppressed by fast moving smaller particles in the size distribution case (Salo et al., 2001). The systematic study of the effects of size distribution on this instability will be conducted in another work.

4. Discussion: Implications for thermal infrared emission of rings

4.1. Fast spin or slow spin?

Thermal emission of rings is a complex function of ring particle properties and ring structure (e.g., Cuzzi et al., 1984; Spilker et al., 2003). One of the biggest issues is whether a particle radiates over its whole surface area or mainly from the face illuminated by direct sunlight, which is the dominant heat source. The former situation may correspond to the case where particle spins are fast compared to the scale of the thermal relaxation time, while the latter corresponds to slowly spinning particles. The rate of post-eclipse temperature increase after emergence from Saturn's shadow suggests that the averaged thermal relaxation time of ring particles is ∼1 h (Froidevaux et al., 1981; Spilker et al., 2003), whereas the orbital period is ∼10 h (in the mid B ring). Therefore, we can roughly say that a particle whose spin frequency is larger than 10Ω is a fast rotator and vice versa.

Fig. 11 shows the spin frequency normalized by the orbital frequency as a function of particle size in various size distribution cases. Both the case including self-gravity and the case without self-gravity are shown. The spin frequency of the largest particles is always close to the orbital frequency, so that their rotation can be considered slow on the scale of a thermal relaxation time. On the other hand, the spin frequency increases with decreasing particle size. Since the spin frequency is roughly proportional to the inverse of particle size, particles smaller than $\sim 0.1 r_{\max}$ are expected to be fast rotators. It should be noted that the total cross section of particles in each logarithmic size bin is the same for the power-law index $q_s = 3$. Therefore, the ratio of the total cross section of fast rotators to that of slow rotators is roughly given by $\sim \log_{10}(r_{\max}/r_{\min}) - 1$. The widths of size distributions estimated from observations, $r_{\max}/r_{\min} \sim 70$–$1000$ (Marouf et al., 1983; French and Nicholson, 2000), suggest that the total cross sections of fast rotators is likely to be comparable to or even larger than that of slow rotators. This appears to be in contrast to the previous thermal models which seem to prefer slow rotators (e.g., Froidevaux, 1981; Kawata, 1983, see also reviews by Cuzzi et al., 1984; Esposito et al., 1984).

Since the solar phase angle dependence of surface temperature is much stronger for slow rotators than that for fast rotators, observations of temperature with various solar phase angles by Cassini will be a strong constraint for the spin state and the width of size distribution of ring particles. In fact, fast rotators can be further classified into two types by their collision frequencies, when considering solar phase angle dependence of their temperature. If the collision frequency is high enough, the illuminated sides of particles change frequently in a random fashion, so that their temperature profile will be close to isothermal. On the other hand, if the collision frequency is small, some fraction of fast rotators have their spin axes directing nearly toward the Sun, so that the phase angle dependence of their temperature is the same as that of a slow rotator. Hence, rings composed of fast rotators with less frequent collisions must have a stronger solar phase angle dependence than rings with frequent collisions. This effect should be included in thermal modeling, besides the other effects related to the optical depth.

4.2. Monolayer or multilayer rings?

So far, two main types of models have been used when investigating the ring's thermal response, namely the monolayer model and the multilayer model. The former type of models explicitly include the effect of finite size of particles, which is important if the particle size is comparable to the mean free path of a photon (i.e., the distance between particles); however the models are limited to a single layer of uni-sized particles (Froidevaux, 1981; Leyrat et al., 2003). On the other hands, the multilayer models solve the classical radiative transfer equations, but neglect the effects of the finite size of particles (Kawata and Irvine, 1975; Kawata, 1983). Interestingly, both types of models can be made consistent with observational data by adjusting various parameters; however, they both prefer slow spins.

The situation of realistic rings suggested by N-body simulations is more complicated. Rings resemble a monolayer for the largest particles since their sizes are comparable to the typical ring thickness ($\sim c/\Omega$), whereas the smaller particles are distributed more extensively in the vertical direction, like assumed in the multilayer models (Fig. 12, top). The importance of the mixed monolayer and multilayer characteristics were already pointed out by optical modeling using particle fields directly obtained by N-body simulations (Salo and Karjalainen, 2003; Salo et al., 2004). Especially, the dependence of the effective

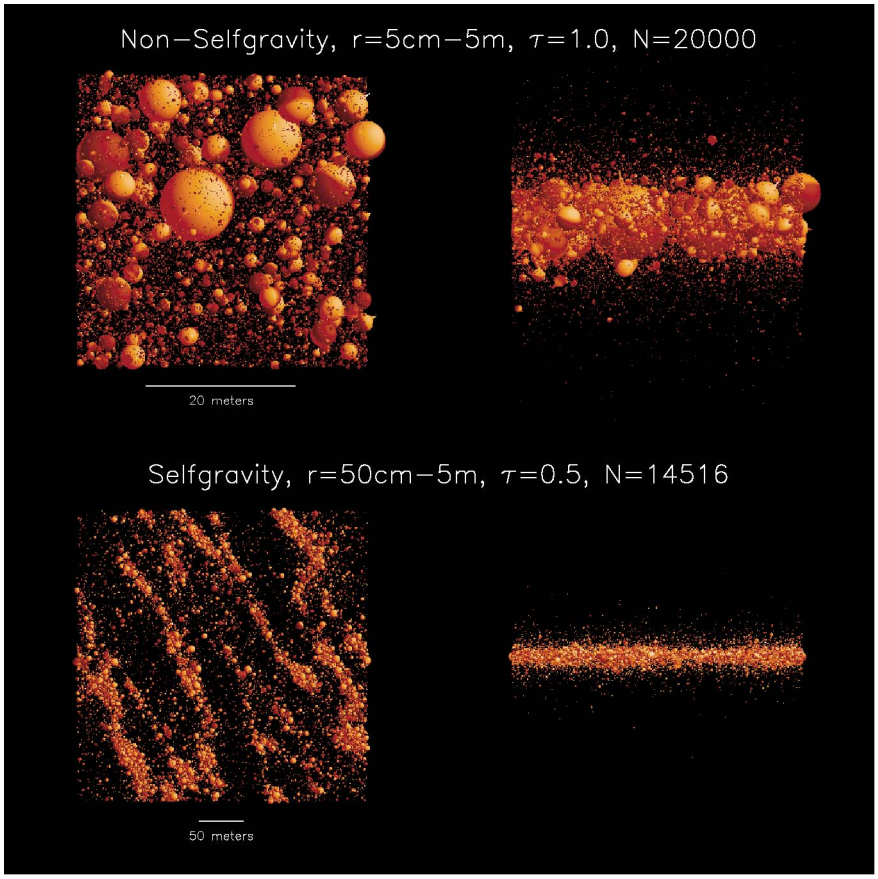

Fig. 12. Examples of simulations without (upper frames) and with (lower frames) self-gravity. Both cases assume $q_s = 3$ and $r_{max} = 5$ m. For the non-self-gravitating case $r_{min} = 5$ cm and $\tau = 1.0$, while $r_{min} = 50$ cm and $\tau = 0.5$ for the self-gravitating case. Left frames display views from the top whereas right frames display views from the side, looking toward the direction of the orbital motion. Northern hemisphere of each particle is colored with brighter color than the southern hemisphere, assuming that the north pole points the direction of the spin axis. Note that the scales used in the upper and lower frames are different.

particle size (and volume density) on the viewing elevation offered an attractive explanation for the optical tilt effect, i.e. the dependence of ring brightness on the elevation. Since the spin state of particles is also sensitive to their size, analogous elevation angle effects might be important in thermal modeling. Further, gravitational wakes cause spatial non-uniformity of ring particles (Fig. 12, bottom), which may also significantly modify their thermal response. It is probably quite difficult to obtain the thermal response of such complicated rings analytically. For the realistic thermal modeling, one may thus need to directly use results of N-body simulations (i.e., particle positions, particle spins).

5. Conclusion

We have investigated the spin state of planetary ring particles using N-body simulations including self-gravity and size distribution. The significant results we obtained are:

1. The spin frequency of the largest particles is close to the orbital frequency regardless of the various ring parameters (i.e., the optical depth, the strength of gravity, or the width of size distribution). Note that by the spin frequency we refer to the dispersion of spins: the spins acquire a non-zero mean vertical component but this is typically insignificant compared to the dispersion.
2. The spin frequency is roughly inversely proportional to the particle size. Thus the spin frequency of small particles is much larger than the orbital frequency, as long as the ring particles possess an extended size distribution.
3. Saturn's ring particles represent a mixture of fast rotators (say $\langle\omega^2\rangle^{1/2} \geqslant 10\Omega$) and slow rotators on the scale of a thermal relaxation time, and the fraction of fast rotators may be comparable to or even exceed that of slow rotators. The future Cassini data of the infrared emission of Saturn's rings, combined with accurate thermal modeling will clarify the fraction of fast rotators. This in turn will constrain the ring particle properties (i.e., the width of size distribution and the particles' thermal inertia).
4. The overall contribution of spins on the dynamical steady-state of rings is not very significant. However, dissipation connected to friction may promote the formation of wakes caused by near-gravitational instability or the formation of axisymmetric oscillations via viscous overstability.

Acknowledgments

We are grateful to Keiji Ohtsuki for his very thoughtful review of the manuscript and for providing preprints of his works. We also thank another reviewer Frank Sphan for most useful comments. This work was supported by the Academy of Finland and the Oulu University special research-unit grant.

Appendix A. Analytic formulation for collisional energy changes

Here ignoring the systematic velocity field, we consider the energy changes due to random motions of particles. We define the kinetic and rotational energies per unit mass as $E_{\rm kin}$ and $E_{\rm rot}$, respectively. The change of these energies $\Delta E_{\rm kin}$ and $\Delta E_{\rm rot}$ in a collision are given by

$$\Delta E_{\rm kin} = \frac{1}{2}\frac{1}{m_1+m_2}\Big[m_1\big(\mathbf{v}_1'^2-\mathbf{v}_1^2\big)+m_2\big(\mathbf{v}_2'^2-\mathbf{v}_2^2\big)\Big], \tag{26}$$

$$\Delta E_{\rm rot} = \frac{1}{5}\frac{1}{m_1+m_2}\Big[m_1 r_1^2\big(\boldsymbol{\omega}_1'^2-\boldsymbol{\omega}_1^2\big)+m_2 r_2^2\big(\boldsymbol{\omega}_2'^2-\boldsymbol{\omega}_2^2\big)\Big]. \tag{27}$$

Using Eqs. (3) and (4), we obtain

$$\Delta E_{\rm kin} = -\frac{1}{2}\frac{m_1m_2}{(m_1+m_2)^2}\bigg[\big(1-\varepsilon_{\rm n}^2\big)\mathbf{u}_{\rm n}^2+\frac{4}{7}(1-\varepsilon_{\rm t})\mathbf{u}_{\rm t}\cdot\mathbf{v}_{\rm r} - \frac{4}{49}(1-\varepsilon_{\rm t})^2\mathbf{u}_{\rm t}^2\bigg], \tag{28}$$

$$\Delta E_{\rm rot} = \frac{m_1m_2}{(m_1+m_2)^2}\bigg[\frac{2}{7}(1-\varepsilon_{\rm t})(\mathbf{n}\times\mathbf{u})\cdot(r_1\boldsymbol{\omega}_1+r_2\boldsymbol{\omega}_2) + \frac{5}{49}(1-\varepsilon_{\rm t})^2(\mathbf{n}\times\mathbf{u})^2\bigg]. \tag{29}$$

We adopt the following assumptions when averaging over collisions (e.g., Salo, 1987a):

1. Impact directions are isotropically distributed. This approximation is valid if the velocity dispersion is much larger than the systematic velocity gradient over particle diameter.
2. The velocity distribution is given by a Maxwellian.
3. There is no correlation between translational and spin motions.

Following these assumptions, the averaged value of $\mathbf{u}_n^2$ as an example is given by

$$\begin{aligned}\big\langle\mathbf{u}_{\rm n}^2\big\rangle &= \frac{\iint f(\mathbf{v}_{\rm r}^3)\mathbf{u}_{\rm n}^2(\mathbf{v}_{\rm r}\cdot\mathbf{n})/|\mathbf{v}_{\rm r}|\,{\rm d}\psi\,{\rm d}\mathbf{v}_{\rm r}^3}{\iint f(\mathbf{v}_{\rm r}^3)(\mathbf{v}_{\rm r}\cdot\mathbf{n})/|\mathbf{v}_{\rm r}|\,{\rm d}\psi\,{\rm d}\mathbf{v}_{\rm r}^3}\\ &= 2\int f\mathbf{v}_{\rm r}^2\,{\rm d}\mathbf{v}_{\rm r}^3\int_0^{\pi/2}\cos^3\theta\sin\theta\,{\rm d}\theta\\ &= \frac{1}{2}\int f\mathbf{v}_{\rm r}^2\,{\rm d}\mathbf{v}_{\rm r}^3 = \frac{2}{3}\big(c_1^2+c_2^2\big),\end{aligned} \tag{30}$$

where $f(\mathbf{v}_{\rm r}^3)$ is the distribution function for $\mathbf{v}_{\rm r}^3$ ($\mathbf{v}_{\rm r}=\mathbf{v}_2-\mathbf{v}_1$) normalized as $\int f(\mathbf{v}_{\rm r}^3)\,{\rm d}\mathbf{v}_{\rm r}^3=1$, ψ is the solid angles for the collisional direction $\mathbf{n}$, and $c_1=\langle\mathbf{v}_1^2\rangle^{1/2}$ and $c_2=\langle\mathbf{v}_2^2\rangle^{1/2}$ are velocity dispersions. Integrations are carried out where impacts are possible, $\mathbf{v}_{\rm r}\cdot\mathbf{n}<0$. In the above equation, the last equality comes from the Maxwellian velocity distribution (see Hämeen-Anttila, 1983). Similar to Eq. (30),

$$\big\langle\mathbf{u}_{\rm t}^2\big\rangle = \frac{2}{3}\big(c_1^2+c_2^2\big)+\frac{2}{3}\big(q_1^2+q_2^2\big), \tag{31}$$

where $q_1=\langle(r_1\boldsymbol{\omega}_1)^2\rangle^{1/2}$ and $q_2=\langle(r_2\boldsymbol{\omega}_2)^2\rangle^{1/2}$ are dispersions of spin velocities.

Finally, we obtain

$$\begin{aligned}\Delta E_{\rm kin} &= -\frac{1}{3}\frac{m_1m_2}{(m_1+m_2)^2}\big(c_1^2+c_2^2\big)\\ &\quad\times\bigg[\big(1-\varepsilon_{\rm n}^2\big)+\frac{4}{7}(1-\varepsilon_{\rm t})-\frac{4}{49}(1-\varepsilon_{\rm t})^2\bigg]\\ &\quad+\frac{4}{147}\frac{m_1m_2}{(m_1+m_2)^2}\big(q_1^2+q_2^2\big)(1-\varepsilon_{\rm t})^2,\end{aligned} \tag{32}$$

$$\begin{aligned}\Delta E_{\rm rot} &= -\frac{m_1m_2}{(m_1+m_2)^2}\big(q_1^2+q_2^2\big)\\ &\quad\times\bigg[\frac{4}{21}(1-\varepsilon_{\rm t})-\frac{10}{147}(1-\varepsilon_{\rm t})^2\bigg]\\ &\quad+\frac{10}{147}\frac{m_1m_2}{(m_1+m_2)^2}\big(c_1^2+c_2^2\big)(1-\varepsilon_{\rm t})^2.\end{aligned} \tag{33}$$

For the case of identical particles, we obtain Eqs. (12) and (13). Equation (33) gives $E_{\rm rot}/E_{\rm kin}$ in the equilibrium state (Eq. (14)), and using this ratio we can obtain the ratio $\langle\mathbf{u}_{\rm t}^2\rangle/\langle\mathbf{u}_{\rm n}^2\rangle$ (Eq. (9)).

Appendix B. Shear rate dependence of the mean spin rate

The non-zero z-component of the mean spin rate is caused by the systematic velocity gradient, which is ignored in Appendix A. Here we briefly review the derivation of the analytic expression for the mean spin rate after Salo (1987a) (see its Section 5 for more detail).

Using Eq. (1), the systematic velocity difference at the contact point $\mathbf{u}_{\rm sy}$ contributed by the systematic velocity gradient is given by

$$\mathbf{u}_{\rm sy} = \mathbf{v}_{\rm sy}-(r_1\boldsymbol{\omega}_1+r_2\boldsymbol{\omega}_2)\times\mathbf{n}. \tag{34}$$

Here $\mathbf{v}_{\rm sy}$ is the velocity gradient in the inertial system give as

$$\mathbf{v}_{\rm sy} = (0,-sx,0)\Omega+(-y,x,0)\Omega, \tag{35}$$

where x and y are the coordinate differences between contacting particles' centers in the radial and azimuth directions, respectively, and s is the normalized shear rate ($s=3/2$ for the Keplerian case). The first and second terms in the right-hand side of Eq. (35) represent the systematic velocity shear in the rotational coordinate and the modification term from the rotational coordinate to the inertial coordinate, respectively.

In the equilibrium state, the mean value of spin change in collisions vanishes, $\langle r_1\boldsymbol{\omega}_1'-r_1\boldsymbol{\omega}_1\rangle=0$. Therefore, from Eq. (4), the following equation needs to be satisfied as well:

$$\langle\mathbf{n}\times\mathbf{v}_{\rm sy}\rangle = (r_1\boldsymbol{\omega}_1+r_2\boldsymbol{\omega}_2)-(r_1\boldsymbol{\omega}_1+r_2\boldsymbol{\omega}_2)\cdot\langle\mathbf{nn}\rangle. \tag{36}$$

Assuming that particle flux is proportional to $\mathbf{v}_{sy} \cdot \mathbf{n}$ and carrying out the averaging where impacts are possible ($\mathbf{v}_{sy} \cdot \mathbf{n} > 0$), we obtain the z-components of averaged values (from Table II of Salo, 1987a)

$$\langle \mathbf{n} \times \mathbf{v}_{sy} \rangle_z = \frac{1}{5}(4-2s)(r_1+r_2)\Omega, \tag{37}$$

$$\langle \mathbf{nn} \rangle_{zz} = \frac{1}{5}\mathbf{I}_{zz}, \tag{38}$$

where $\mathbf{I}$ is the unit tensor. Substituting these values into Eq. (36), we obtain the equilibrium spin rate $\langle w_z \rangle_{ana} = 1/4(4-2s)\Omega$ for the identical particle case.

If we assume random impacts supposing large velocity dispersion cases, we obtain

$$\langle \mathbf{nn} \rangle_{zz} = \frac{1}{3}\mathbf{I}_{zz}. \tag{39}$$

If we use this value instead of Eq. (38), we obtain slightly higher value:

$$\langle w_z \rangle_{ana} = 0.3(4-2s)\Omega. \tag{40}$$

This shear rate dependence is used for the analysis in Section 3.2.

As one can see, we do not consider each collision orbit precisely and the averaging is not well consistent for different terms for large velocity dispersion cases. On the other hand, Ohtsuki (2004a, 2004b) obtained the mean spin rate analytically by averaging the torque exerted by all the non-circular collision orbits precisely, but only for the Keplerian shear case. His obtained spin rate ($\langle w_z \rangle_{ana} \simeq 0.37$) is slightly higher than ours (0.3). The extension of Ohtsuki's method to various shear rates would be helpful for more accurate analysis.

Appendix C. Required total number of particles for size distribution cases

For the size distribution case, the number of particles $N(r)$ with radii between r and $r+\mathrm{d}r$ is assumed to be $N(r) = Ar^{-q_s}$, with the upper and lower cutoffs r_{max} and r_{min}, where A is a constant. For a larger q_s and a larger width $W = r_{max}/r_{min}$, the required number of particles in simulations increases.

Let us first consider physical quantities in a simulation box with the area of L^2. The total number of particles N_{tot} is given by

$$N_{tot} = A\int_{r_{min}}^{r_{max}} n(r)\,\mathrm{d}r = \frac{Ar_{max}^{1-q_s}}{1-q_s}\left(1 - W^{q_s-1}\right). \tag{41}$$

Since we divide particles into groups with a constant logarithmic size increment $\Delta W = 10^{1/6}$, the number of particles in the group of the largest particles becomes

$$N_L = N_{tot}\frac{1-10^{(q_s-1)/6}}{1-W^{q_s-1}}, \tag{42}$$

where we used Eq. (41). The total optical depth τ is given by

$$\tau = \frac{\pi}{L^2}\frac{Ar_{max}^{3-q_s}}{3-q_s}\left(1-W^{q_s-3}\right) = \frac{\pi r_{max}^2}{L^2}N_{tot}F_1, \tag{43}$$

where $F_1 = \frac{1-q_s}{3-q_s}\frac{1-W^{q_s-3}}{1-W^{q_s-1}}$ (for the case of $q_s = 3$, the factor $(1-W^{q_s-3})/(3-q_s)$ is replaced by $\ln W$). The total surface density is given by

$$\Sigma = \frac{4\pi\rho}{3L^2}\frac{Ar_{max}^{4-q_s}}{4-q_s}\left(1-W^{q_s-4}\right) = \frac{4}{3}\rho\tau r_{max}F_2, \tag{44}$$

where $F_2 = \frac{3-q_s}{4-q_s}\frac{1-W^{q_s-4}}{1-W^{q_s-3}}$ and we used Eq. (43) for the transformation. The velocity dispersion can be scaled by $r_{eff}\Omega$, where $r_{eff} = r_{max}F_2$ is the effective radius (see Section 3.3).

The first condition for the required total particle number is determined by the minimum number of particles in the group of the largest particles (Salo, 1992a). From Eq. (42), we obtain

$$N_{ng,1} = \frac{1-W^{q_s-1}}{1-10^{(q_s-1)/6}}N_L. \tag{45}$$

Taking $N_L = 5$ as the smallest statistically meaningful number of 'largest' particles, with $q_s = 3$ and $W = 100$, it gives $N_{ng,1} = 21{,}400$. The second condition is determined by the minimum size ratio of the simulation box size L to the largest particle size (Salo, 1992a). From Eq. (43), we obtain

$$N_{ng,2} = \left(\frac{L}{r_{max}}\right)^2\frac{\tau}{\pi F_1}. \tag{46}$$

For $\tau = 1.0$, $q_s = 3$, $W = 100$, and $L/r_{max} = 8$, we obtain $N_{ng,2} = 22{,}100$. The above two conditions give almost the same required number if $\tau = 1.0$. For larger τ, the second condition becomes more severe.

For dense self-gravitating rings, wakes form due to near-gravitational instability. The radial scale of wakes is expected to be comparable to the critical wave length λ_{crit}:

$$\lambda_{crit} = 4\pi^2 G\Sigma/\Omega^2. \tag{47}$$

The third condition for the required total particle number is determined by the ratio of λ_{crit} to the simulation box size L. From Eqs. (43), (44), and (47), we obtain

$$N_{wake} = 2210\tau^3\left(\frac{a}{10^8\ \mathrm{m}}\right)^6\left(\frac{\rho}{900\ \mathrm{kg\,m^{-3}}}\right)^2\left(\frac{L}{\lambda_{crit}}\right)^2 F_2^2/F_1. \tag{48}$$

This is much more severe than other two conditions unless τ is much smaller than unity. Since the simulation results are almost independent of the simulations box size for $L > 4\lambda_{crit}$ (Salo, 1995), we adopt $L = 4\lambda_{crit}$ for obtaining the minimum particle number for a self-gravitating simulation. From the above equation, one can find that the required number for a size distribution case is $F_3 = F_2^2/F_1$ times larger than that for a case of identical particles with the same condition. If $q_s = 3$, $F_3 = 3.3$ and 50.2 for $W = 10$ and 100, respectively.

References

Araki, S., 1988. The dynamics of particle disks. II. Effects of spin degrees of freedom. Icarus 76, 182–198.

Araki, S., 1991. The dynamics of particle disks. III. Dense and spinning particle disks. Icarus 90, 139–171.

Araki, S., Tremaine, S., 1986. The dynamics of particle disks. Icarus 65, 83–109.

Aumann, H.H., Kieffer, H.H., 1973. Determination of particle sizes in Saturn's rings from their eclipse cooling and heating curves. Astrophys. J. 186, 305–311.

Brahic, A., 1977. Systems of colliding bodies in a gravitational field. I. Numerical simulation of the standard model. Astron. Astrophys. 54, 895–907.

Brilliantov, N.V., Spahn, F., Hertzsch, J., Pöschel, T., 1996. Model for collisions in granular gases. Phys. Rev. E 53, 5382–5392.

Collwell, J.E., Esposito, L.W., Sremčević, M., 2005. Gravitational wake structure in Saturn's rings from multiple stellar occultations. Bull. Am. Astron. Soc. 37, 763.

Cuzzi, J.N., Lissauer, J.J., Esposito, L.W., Holberg, J.B., Marouf, E.A., Tyler, G.L., Boishot, A., 1984. Saturn's rings: Properties and processes. In: Greenberg, R., Brahic, A. (Eds.), Planetary Rings. Univ. of Arizona Press, Tucson, pp. 73–199.

Daisaka, H., Ida, S., 1999. Spatial structure and coherent motion in dense planetary rings induced by self-gravitational instability. Earth Planets Space 51, 1195–1213.

Daisaka, H., Tanaka, H., Ida, S., 2001. Viscosity in a dense planetary ring with self-gravitating particles. Icarus 154, 296–312.

Esposito, L.W., Cuzzi, J.N., Holberg, J.B., Marouf, E.A., Tyler, G.L., Porco, C.C., 1984. Saturn's rings: Structure, dynamics, and particle properties. In: Gehrels, T., Matthews, M.S. (Eds.), Saturn. Univ. of Arizona Press, Tucson, pp. 463–544.

Ferrari, C., Spilker, L., Brooks, S., Edgington, S.G., Pearl, J., Leyrat, C., Flasar, M., CIRS Investigation Team, 2005. Azimuthal temperature variations in Saturn's rings as seen by the CIRS spectrometer onboard Cassini. Bull. Am. Astron. Soc. 37, 764.

French, R.G., Nicholson, P.D., 2000. Saturn's rings. II. Particle sizes inferred from stellar occultation data. Icarus 145, 502–523.

Froidevaux, L., 1981. Saturn's rings: Infrared brightness variation with solar elevation. Icarus 46, 4–17.

Froidevaux, L., Matthews, K., Neugbauer, G., 1981. Thermal response of Saturn's ring particles during and after eclipse. Icarus 46, 18–26.

Goldreich, P., Tremaine, S., 1978. The velocity dispersion in Saturn's rings. Icarus 34, 227–239.

Goldreich, P., Tremaine, S., 1982. The dynamics of planetary rings. Ann. Rev. Astron. Astrophys. 20, 249–283.

Hämeen-Anttila, K.A., 1978. An improved and generalized theory for the collisional evolution of Keplerian systems. Astrophys. Space Sci. 58, 477–520.

Hämeen-Anttila, K.A., 1983. Collisions in self-gravitating clouds of planetesimals. Earth Moon Planets 28, 267–303.

Hämeen-Anttila, K.A., 1984. Collisional theory of non-identical particles in a gravitational field. Earth Moon Planets 31, 271–299.

Hämeen-Anttila, K.A., Lukkari, J., 1980. Numerical simulations of collisions in Keplerian systems. Astrophys. Space Sci. 71, 475–497.

Hämeen-Anttila, K.A., Salo, H., 1993. Generalized theory of impacts in particulate systems. Earth Moon Planets 62, 47–84.

Hänninen, J., Salo, H., 1992. Collisional simulations of satellite Lindblad resonances. Icarus 97, 228–247.

Hänninen, J., Salo, H., 1994. Collisional simulations of satellite Lindblad resonances. II. Formation of narrow ringlets. Icarus 108, 325–346.

Hänninen, J., Salo, H., 1995. Formation of isolated narrow ringlets by a single satellite. Icarus 117, 435–438.

Huber, D., Pfenniger, D., 2001. Lumpy structures in self-gravitating disks. Astron. Astrophys. 374, 465–493.

Julian, W.H., Toomre, A., 1966. Non-axisymmetric responses of differentially rotating disks of stars. Astrophys. J. 146, 810–830.

Karjalainen, R., Salo, H., 2004. Gravitational accretion of particles in Saturn's rings. Icarus 172, 328–348.

Kawata, Y., 1983. Infrared brightness temperature of Saturn's rings based on the inhomogeneous multilayer assumption. Icarus 56, 453–464.

Kawata, Y., Irvine, W.M., 1975. Thermal emission from a multiple scattering model of Saturn's rings. Icarus 24, 472–482.

Lewis, M.C., Stewart, G.R., 2000. Collisional dynamics of perturbed planetary rings. Astron. J. 120, 3295–3310.

Lewis, M.C., Stewart, G.R., 2005. Expectations for Cassini observations of ring material with nearby moons. Icarus 178, 124–143.

Leyrat, C., Ferrari, C., Spilker, L., Charnoz, S., 2003. Thermal radiation from Saturn's rings: New results on the spin of particles. Bull. Am. Astron. Soc. 35. 20.06.

Lukkari, J., 1978. Numerical simulations of colliding particles in a gravitational field. Astron. Space Sci. 58, 113–123.

Marouf, E.A., Tyler, G.L., Zebker, H.A., Simpson, R.A., Eshleman, V.R., 1983. Particle size distributions in Saturn's rings from Voyager 1 radio occultation. Icarus 54, 189–211.

Morishima, R., Salo, H., 2004a. Spin rates of small moonlets embedded in planetary rings. I. Three-body calculations. Icarus 167, 330–346.

Morishima, R., Salo, H., 2004b. Simulations of dense planetary rings: Rotating self-gravitating particles with size distribution. Bull. Am. Astron. Soc. 36. 19.01.

Mosqueira, I., 1996. Local simulations of perturbed dense planetary rings. Icarus 122, 128–152.

Nicholson, P.D., Hedman, M.M., Wallis, B., 2005. Cassini-VIMS observations of stellar occultations by Saturn's rings. Bull. Am. Astron. Soc. 37, 763–764.

Ohtsuki, K., 1993. Capture probability of colliding planetesimals: Dynamical constraints on accretion of planets, satellites and ring particles. Icarus 106, 228–246.

Ohtsuki, K., 1999. Evolution of particle velocity dispersion in a circumplanetary disk due to inelastic collisions and gravitational interactions. Icarus 137, 152–177.

Ohtsuki, K., 2004a. Formulation and analytic calculation for the spin angular momentum of a moonlet due to inelastic collisions of ring particles. Earth Planets Space 56, 909–919.

Ohtsuki, K., 2004b. On the rotation of a moonlet embedded in planetary rings. Icarus 172, 432–445.

Ohtsuki, K., 2005. Rotation rates of particles in Saturn's rings. Astrophys. J. 626, L61–L64.

Ohtsuki, K., Emori, H., 2000. Local N-body simulations for the distribution and evolution of particle velocities in planetary rings. Astron. J. 119, 403–416.

Ohtsuki, K., Toyama, D., 2005. Local N-body simulations for the rotation rates of particles in planetary rings. Astrophys. J. 130, 1302–1310.

Petit, J.-M., Hénon, M., 1987. A numerical simulation of planetary rings. Astron. Astrophys. 173, 389–404.

Richardson, D.C., 1994. Tree code simulations of planetary rings. Mon. Not. R. Astron. Soc. 269, 493–511.

Salo, H., 1985. Numerical simulations of collisions and gravitational encounters in systems of non-identical particles. Earth Moon Planets 33, 189–200.

Salo, H., 1987a. Collisional evolution of rotating, non-identical particles. Earth Moon Planets 38, 149–181.

Salo, H., 1987b. Numerical simulations of collisions between rotating particles. Icarus 70, 37–51.

Salo, H., 1991. Numerical simulations of dense collisional systems. Icarus 90, 254–270.

Salo, H., 1992a. Numerical simulations of dense collisional systems. II. Extended distribution of particle sizes. Icarus 96, 85–106.

Salo, H., 1992b. Gravitational wakes in Saturn's rings. Nature 359, 619–621.

Salo, H., 1995. Simulations of dense planetary rings. III. Self-gravitating identical particles. Icarus 117, 287–312.

Salo, H., 2000. Numerical simulations of collisional dynamics of planetary rings. In: Pöschel, T., Luding, S. (Eds.), Granular Gases. In: Lecture Notes in Physics, vol. 564. Springer-Verlag, Berlin, pp. 330–349.

Salo, H., Karjalainen, R., 2003. Photometric modeling of Saturn's rings. I. Monte Carlo method and the effect of nonzero volume filling factor. Icarus 164, 428–460.

Salo, H., Schmidt, J., Spahn, F., 2001. Viscous overstability in Saturn's B ring. I. Direct simulations and measurement of transport coefficients. Icarus 153, 295–315.

Salo, H., Karjalainen, R., French, R.G., 2004. Photometric modeling of Saturn's rings. II. Azimuthal asymmetry in reflected and transmitted light. Icarus 170, 70–90.

Schmidt, J., Salo, H., 2003. Weakly non-linear model for oscillatory instability in Saturn's dense rings. Phys. Rev. Lett. 90. 061102(1–4).

Schmidt, J., Salo, H., Petzschmann, O., Spahn, F., 1999. Vertical distribution of temperature and density in a planetary ring. Astron. Astrophys. 345, 646–652.

Schmidt, J., Salo, H., Spahn, F., Petzschmann, O., 2001. Viscous overstability in Saturn's B ring. II. Hydrodynamic theory and comparison to simulations. Icarus 153, 316–331.

Schmit, U., Tscharnuter, W.M., 1999. On the formation of the fine-structure in Saturn's B ring. Icarus 138, 173–187.

Seiss, M., Spahn, F., Sremčević, M., Salo, H., 2005. Structures induced by small moonlets in Saturn's rings: Implications for the Cassini Mission. Geophys. Res. Lett. 32. L11205.

Shu, F.H., Dones, L., Lissauer, J.J., Yuan, C., Cuzzi, J.N., 1985. Nonlinear spiral density waves: Viscous damping. Astrophys. J. 299, 542–573.

Shukhman, I.G., 1984. Collisional dynamics of particles in Saturn's rings. Sov. Astron. 28 (5), 574–585.

Spahn, F., Sremčević, M., 2000. Density patterns induced by small moonlets in Saturn's rings? Astron. Astrophys. 358, 368–372.

Spahn, F., Schmidt, J., Petzschmann, O., Salo, H., 2000. Stability analysis of a Keplerian disk of granular grains: Influence of thermal diffusion. Icarus 145, 657–660.

Spahn, F., Scholl, H., Hertzsch, J., 1994. Structures in planetary rings caused by embedded moonlets. Icarus 111, 514–535.

Spilker, L., Ferrari, C., Showalter, M., Cuzzi, J.N., Pearl, J., Wallis, B., 2003. Saturn's rings in the thermal infrared. Planet. Space Sci. 51, 929–935.

Stewart, G.R., Lin, D.N.C., Bodenheimer, P., 1984. Collision-induced transport processes in planetary rings. In: Greenberg, R., Brahic, A. (Eds.), Planetary Rings. Univ. of Arizona Press, Tucson, pp. 447–512.

Sremčević, M., Spahn, F., Duschl, W.J., 2002. Density structures in perturbed thin cold discs. Mon. Not. R. Astron. Soc. 337, 1139–1152.

Supulver, K.D., Bridges, F.G., Lin, D.N.C., 1995. The coefficient of restitution of ice particles in glancing collisions: Experimental results for unfrosted surfaces. Icarus 113, 188–199.

Tanaka, H., Ohtsuki, K., Daisaka, H., 2003. A new formulation of the viscosity in planetary rings. Icarus 161, 144–156.

Toomre, A., 1964. On the gravitational stability of a disk of stars. Astrophys. J. 139, 1217–1238.

Toomre, A., Kalnajs, A.J., 1991. Spiral chaos in an orbital patch. In: Sundelius, B. (Ed.), Dynamics of Disk Galaxies. Univ. Chalmers Press, Göteborg, pp. 341–358.

Trulsen, J., 1972. Numerical simulation of jetstreams. Astrophys. Space Sci. 17, 241–262.

Wisdom, J., Tremaine, S., 1988. Local simulations of planetary rings. Astron. J. 95, 925–940.